Engineering with Computers (2023) 39:575–606
https://doi.org/10.1007/s00366-022-01616-7

ORIGINAL ARTICLE

Peridynamic modeling and simulation of thermo-mechanical fracture in inhomogeneous ice

Ying Song[1] · **Shaofan Li**[2] · **Yunbo Li**[1]

Received: 12 October 2021 / Accepted: 22 January 2022 / Published online: 19 February 2022

Abstract

It is challenging to build a physically accurate sea ice model, which is highly sensitive to temperature and many uncertain factors, such as its nonuniform and inhomogeneous microstructure. In this work, we adopt a peridynamics approach to develop an inhomogeneous sea ice model and applied it to simulate crack propagation in a thermo-mechanical field of ice sheet. To develop an inhomogeneous ice model, we treat the critical stretch of inhomogeneous ice material as a random variable that obeys the Weibull distribution. A coupled thermo-mechanical peridynamics approach is adopted to simulate ice crack propagation, and a key component of this approach is adopted the temperature-dependent critical stretch. Thus, we can model the temperature-dependent crack propagation. Moreover, the wing crack growth problem is simulated to demonstrate the accuracy of the proposed inhomogeneous peridynamics ice model, whose simulation results agree well with the experimental data. Furthermore, the influence of the initial crack length, temperature, and bubbles in ice were also studied to understand the microcrack formation mechanism in ice. The results of this work show that the proposed peridynamic ice model not only provides an efficient tool to simulate the complex deformation pattern in ice failure process in a coupled thermo-mechanical field, but also reveals the mechanical mechanism of fracture in ice.

Keywords Crack · Fracture · Inhomogeneous ice · Peridynamics · Thermo-mechanical coupling · Weibull distribution

List of symbols

$\boldsymbol{\xi}_{\mathrm{AB}}$	The bond vector of material point $\mathbf{x}_{\mathrm{A}}$ and $\mathbf{x}_{\mathrm{B}}$ in reference configuration
$\boldsymbol{\eta}_{\mathrm{AB}}$	The relative displacement vector of material point $\mathbf{x}_{\mathrm{A}}$ and $\mathbf{x}_{\mathrm{B}}$ in current configuration
c_v	The specific heat capacity
h_s	The heat generate rate
$\Theta(\mathbf{x}_{\mathrm{A}}, t)$	The temperature at material point $\mathbf{x}_{\mathrm{A}}$
θ_{AB}	The temperature difference between material point $\mathbf{x}_{\mathrm{A}}$ and $\mathbf{x}_{\mathrm{B}}$
$H_{x_{\mathrm{A}}}$	The horizon of particle $\mathbf{x}_{\mathrm{A}}$
$\mathbf{f}(\boldsymbol{\xi}, \boldsymbol{\eta}, t)$	The body force density function
f_h	The heat flow density function
μ_h	The bond history function
ϕ_h	The failure function index
s	The bond stretch
s_0	The critical bond stretch
c	The micro-modulus
$f_h(\Theta_{\mathrm{B}} - \Theta_{\mathrm{A}}, \mathbf{x}_{\mathrm{B}} - \mathbf{x}_{\mathrm{A}}, t)$	The thermal bond force density
$\kappa(\mathbf{x}_{\mathrm{A}}, \mathbf{x}_{\mathrm{B}})$	The micro-conductivity of the thermal bond
$K(\mathbf{x}_{\mathrm{A}}, \mathbf{x}_{\mathrm{B}})$	The thermal conductivity of the material
G_0	The energy release rate
K_I	The fracture toughness
s^{TH}	Thermo-mechanical bond stretch
s_0^{TH}	Thermo-mechanical bond critical stretch
s_i^{TH}	The critical stretch variable
$\overline{s_i}^{\mathrm{TH}}$	The average critical stretch
m	The shape parameter
$f\left(s_i^{\mathrm{TH}}, \overline{s_i}^{\mathrm{TH}}, m\right)$	The probability density distribution function

✉ Shaofan Li
shaofan@berkeley.edu

[1] College of Ocean Science and Engineering, Shanghai Maritime University, Shanghai 200135, China

[2] Department of Civil and Environmental Engineering, University of California, Berkeley, USA

$F\left(s_i^{\mathrm{TH}}, \overline{s}_i^{\mathrm{TH}}, m\right)$	The probability distribution function
p	The porosity of ice

1 Introduction

Sea ice is undoubtedly one of the most complex natural composite materials in nature, and it is formed by freezing seawater in a low-temperature environment (see Fig. 1). Sea ice is a mixture of solid ice crystals, salt inclusions, and a few air bubbles [59]. The microstructure of polar sea ice greatly affects its macroscopic mechanical properties [38]. From the microscale perspective, the macroscopic material properties of ice are delineated by grain size [31], crystal orientation, porosity, salt content, defect structure, nucleation, and movement [51]. From a macroperspective, sea ice is a nonuniform and anisotropic viscous material [14], which is usually affected by temperature change [12] and loading rate [10]. Study of the microstructure characteristics and macroscopic mechanical responses of sea ice will help us understand physical failure processes and mechanisms of sea ice. To date, numerical modeling and prediction of the complex behaviors of ice under the thermo-mechanical field is not only still an open problem in the cold regions science, and the related computational simulation is still a challenge in the field of computational mechanics.

To develop an appropriate sea ice model, much effort has been made in the past decades. Various experiments and tests had been taken on studying the mechanical behaviors of ice. According to the research of Petrovic et al. [39], whether it is undercompression or tension, the strength of ice increases with decreasing temperature. In particular, the compressive strength of ice is more affected by temperature than its tensile strength. Haynes [12] showed that the compressive strength increased by approximately 8 tines strength when the temperature changes from −0.1 to −54 °C. However, Haynes also pointed out that within the same temperature range, the tensile strength increased by approximately 3 times during the same among temperature change. Schulson [50] studied the relationship between the compressive strength of ice and temperature, which is caused by the dislocation of ice crystals and the slip phenomenon between particles. These results [21] indicated the importance of temperature effects in building the ice model.

Fig. 1 Sea ice in the Arctic Ocean. (Photo Courtesy: Pink floyd88/ Wikimedia Commons)

However, the preparation of the ice sample for experiment requires a certain amount of manpower, financial resources [5, 7], and time on site and material preparation [6, 19]. Thus, it is necessary to carry out numerical simulation to save resources and improve efficiency [36, 37]. The ice breaking process is a material destruction process from continuous to discrete. The difficulty of numerical simulations is how to deal with the transition from continuous to discontinuous. Using the traditional continuum mechanics method, theoretically, it is required to obtain the derivatives to solve the partial differential equations, which may lead to the singularity when calculating spatial derivatives near the crack tip. For example, the finite-element (FEM) approach (see Li et al. [22]) needs to judge the location as well as the size of cracks. The extended finite-element method (XFEM) Xu et al. [67] introduced the discontinuous shape function and additional degrees of freedom to solve the crack problem. One may also use the meshfree particle method to model fracture, e.g., [23, 34, 35, 40, 43], which needs to implement visibility condition to grow cracks. Recently, the phase-field method has been applied to fracture, as well, e.g., [3, 44]; however, the phase-field method may not be the best approach in simulation fracture in porous media.

On the other hand, the development of macroscale constitutive model for ice started in the 1970s, in which the influences of microstructure of the ice were often ignored. For the large- and medium-scale sea ice in the polar regions, Hibler [13] developed a viscoplastic sea ice constitutive model, and Hunke et al. [15] applied a viscoelastic–plastic thermodynamic model to analyze the mechanical responses of ice to wind loads. Aiming at sea ice with small strain rate and small deformation, Ji et al. [16] established a viscoelastic–plastic sea ice dynamic constitutive model in the framework of discrete element method (DEM), and they simulate the dynamic responses of sea ice under different types and scales by adjusting parameters such as elastic modulus and cohesive force. On this basis, Pan et al. [33] employed the smoothed particle hydrodynamics (SPH) method study of ice-sheet and ice-shelf dynamics. In summary, the DEM method and SPH method [57, 58, 60, 61] and their coupling method have successfully applied solving ice hydrodynamics and provided prediction in broken ice areas. However, the coupling method of DEM and SPH does not consider

ice fracture and fragmentation process. To simulate fracture process in ice materials, we need a method that can accurately model and simulate complex crack propagation process in ice.

Peridynamics (PD) method proposed by Silling [52] has some advantages in simulating the material failure such as discontinuity in displacement or crack propagation. In peridynamics, it is assumed that the interaction between two adjacent material points in the material may be described by a bond force, and the overall effects of such bond forces on a material point can be described by nonlocal differential operators as forms of integral equations, instead of partial differential equations [1, 28, 42, 72]. In doing so, the solution space has enlarged, which includes the discontinuous solutions [53]. In recent years, peridynamics has been developed rapidly [46]. It has been applied to solve many engineering problems [29] in material failure analysis [45] as well as multi-physics modeling [30]; such as impact and penetration of composite materials, fracture in rock cracks [41], concrete damage, and others; dual-horizon peridynamics for dealing with a nonuniform horizon for each particle [47, 48]. It is worth mentioning that peridynamics can also be applied to simulate ice crack propagation, such as the interaction of ice and propeller in the process of ice cutting by a propeller (see Ye et al. [69, 70] and Xiong et al. [66]); ice breaking process in the icebreaking process of an icebreaker (see Liu et al. [25, 26] and Xue et al. [68]); ice destruction process under the action of underwater explosion load, e.g., Wang et al. [62]. Moreover, Lu et al. [27] developed a peridynamic approach to model polycrystalline ice by introducing the crystal boundary coefficient into the critical elongation expression of peridynamics formulation and applied it to simulate the microscopic crack initiation process of polycrystalline ice. With the developments of these studies, our understanding and knowledge of ice and its mechanical responses have been continuously improved. However, in the existing literature, concerning the modeling and simulation of ice fracture and fragmentation, to the best of authors' knowledge, no ice constitutive model that considers both the temperature and microstructure effect has been developed. The related research on the destruction process of ice in the thermo-mechanical coupling field [2, 8, 11, 32, 64] is scarce.

There were some inhomogeneous ice models available in the literature, such as the work by Wang et al. [63, 65], and they used the Weibull random distribution function in peridynamics to study brittle geotechnical materials. Zhang et al. [73] proposed a peridynamic model to study the heterogeneous rock-like brittle materials based on the Weibull distribution function. Jones et al. [17, 18] simulated the nonhomogeneous brittle material by introducing the critical elongation into the Weibull random distribution function. Based on this argument, in this work, we introduced a critical elongation with a temperature random variable that obeys the Weibull distribution to simulate nonhomogeneous ice. Besides, the microscopic physical properties and mechanical mechanism are studied, as well.

In this work, we focus on developing a coupled thermo-mechanical ice model that considers the microstructure effect and is capable of simulating fracture. To provide an accurate numerical or computational model to simulate ice cracking process in a complex thermo-mechanical field, we used a fully coupled thermo-mechanical bond-based peridynamics to build a nonhomogeneous ice model.

The rest of paper is organized as follows: first, in Sect. 2, we present a probabilistic mechanics model for heterogeneous sea ice based on the Weibull distribution function and the thermo-mechanical coupled bond-based peridynamics. Second, by employing the proposed inhomogeneous ice model, we simulated the wing crack propagation in ice to validate the proposed numerical model, and then, we presented and analyzed the simulation results that take into account the influence of initial defects, grain size, temperature, and bubble effects in Sect. 3. Finally, in Sect. 4, we conclude the work with discussions and perspectives.

2 Inhomogeneous ice model in the framework of coupled thermo-mechanical bond-based peridynamics

Sea ice is a natural composite material. Due to the environmental impact on its formation process, the composition of ice is relatively complex, including air, salt, impurities, etc. Different types of sea ice have different material properties and mechanical properties. Multi-year ice can be simplified as an isotropic material due to its regular arrangement of crystal structure, while the arrangement of new ice, especially columnar ice crystals, has a certain directionality and can be regarded as an anisotropic material. The internal structure of ice is unevenly distributed and can be regarded as a kind of nonhomogeneous composite materials. To simplify calculations, traditional theoretical models often regard ice as homogeneous and continuous distributed isotropic materials, which has some serious limitations. To deal with it, a constitutive model of heterogeneous ice materials is established based on the bond-based peridynamics in this section.

2.1 Thermo-mechanical bond-based peridynamic model for ice

In this work, we applied the bond-based peridynamics to simulate such complex mechanical behavior of sea ice, which considered the temperature, grain size, and the

loading rate. In this work, the ice material can be discretized into several material points $\mathbf{x}_A$, $\mathbf{x}_B$, and the material points are connected by the action of "bonds" within the nonlocal horizon size δ , as shown in Fig. 2. Under the condition of external force, the ice is first deformed, and the "bond" connecting the two material points $\mathbf{x}_A$ and $\mathbf{x}_B$ will then be stretched under the force between the two material points. On the other hand, if the external environment temperature $\Theta(\mathbf{x}_A, t)$, $\Theta(\mathbf{x}_B, t)$ of the ice changes, there is a temperature difference θ_{AB} between the two material points $\mathbf{x}_A$ and $\mathbf{x}_B$ within the deformed ice. This temperature difference θ_{AB} between the material points $\mathbf{x}_A$ and $\mathbf{x}_B$ can be modeled by the temperature bond, denoted as the "t-bond".

Considering the influence of the temperature, the numerical model of sea ice is established within the framework of thermo-mechanical peridynamics. The equation of motion can be expressed as follows:

$$\rho(\mathbf{x}_A)\ddot{\mathbf{u}}(\mathbf{x}_A, t) = \int_{H_A} \mathbf{f}(\boldsymbol{\xi}_{AB}, \boldsymbol{\eta}_{AB}, \theta_{AB}, t)dV_B + \mathbf{b}(\mathbf{x}_A, t), \quad (1)$$

where $\rho(\mathbf{x}_A)$ is the density of the ice, $\ddot{\mathbf{u}}(\mathbf{x}_A, t)$ is the acceleration; $\boldsymbol{\xi}_{AB}$ is the relative position vector of the bond AB; $\boldsymbol{\eta}_{AB}$ is the deformation of the bond AB; $\mathbf{b}(\mathbf{x}_A, t)$ is the external body force acting on the material point $\mathbf{x}_A$, and the induced the bond force density vector is defined as

$$\mathbf{f}(\boldsymbol{\xi}_{AB}, \boldsymbol{\eta}_{AB}, \theta_{AB}, t) = g(\boldsymbol{\xi}_{AB}, \boldsymbol{\eta}_{AB}, \theta_{AB}, t)\mu(\boldsymbol{\xi}_{AB}, \boldsymbol{\eta}_{AB}, \theta_{AB}, t) \cdot \frac{\boldsymbol{\xi}_{AB} + \boldsymbol{\eta}_{AB}}{|\boldsymbol{\xi}_{AB} + \boldsymbol{\eta}_{AB}|}, \quad (2)$$

where $g(\boldsymbol{\xi}_{AB}, \boldsymbol{\eta}_{AB}, \theta_{AB}, t)$ is a linear scalar function representing the magnitude of bond force density, which can be written as

$$g(\boldsymbol{\xi}_{AB}, \boldsymbol{\eta}_{AB}, \theta_{AB}, t) = c(s - \alpha\theta_{AB}), \quad (3)$$

in which c is the micromodule for the material

$$c = \frac{12E}{\pi\delta^4}, \quad (4)$$

α is the thermal expansion coefficient of the material, and θ_{AB} is the temperature difference between the material point, and

$$s = \frac{|\boldsymbol{\xi}_{AB} + \boldsymbol{\eta}_{AB}| - |\boldsymbol{\xi}_{AB}|}{|\boldsymbol{\xi}_{AB} + \boldsymbol{\eta}_{AB}|}, \quad (5)$$

is the bond stretch, and $\mu(\boldsymbol{\xi}_{AB}, \boldsymbol{\eta}_{AB}, \theta_{AB}, t)$ is the bond characteristic function. In passing, we note that

$$\mathbf{n} = \frac{\boldsymbol{\xi}_{AB} + \boldsymbol{\eta}_{AB}}{|\boldsymbol{\xi}_{AB} + \boldsymbol{\eta}_{AB}|},$$

is the direction of the bond force, which is along the direction of the deformed bond position vector.

The peridynamic thermal diffusion equation can be written as follows:

$$\rho(\mathbf{x}_A)c_v(\mathbf{x}_A)\dot{\Theta}(\mathbf{x}_A, t) = \int_{H_A} f_h(\Theta_B - \Theta_A, \mathbf{x}_B - \mathbf{x}_A, t) \mu_h(\boldsymbol{\xi}_{AB}, \boldsymbol{\eta}_{AB}, \theta_{AB}, t)dV_B + h_s(\mathbf{x}_A, t). \quad (6)$$

Here, θ_{AB} denotes the temperature difference between the material point $\mathbf{x}_A$ and $\mathbf{x}_B$, $\Theta(\mathbf{x}_A, t)$, $\Theta(\mathbf{x}_B, t)$ denotes the temperature of the material point $\mathbf{x}_A$ and $\mathbf{x}_B$. $c_v(\mathbf{x}_A)$ denotes the specific heat capacity of material, $h_s(\mathbf{x}_A, t) = \rho_0 s_b$ represents the heat generation rate.

The thermal bond force density are defined as follows [54]:

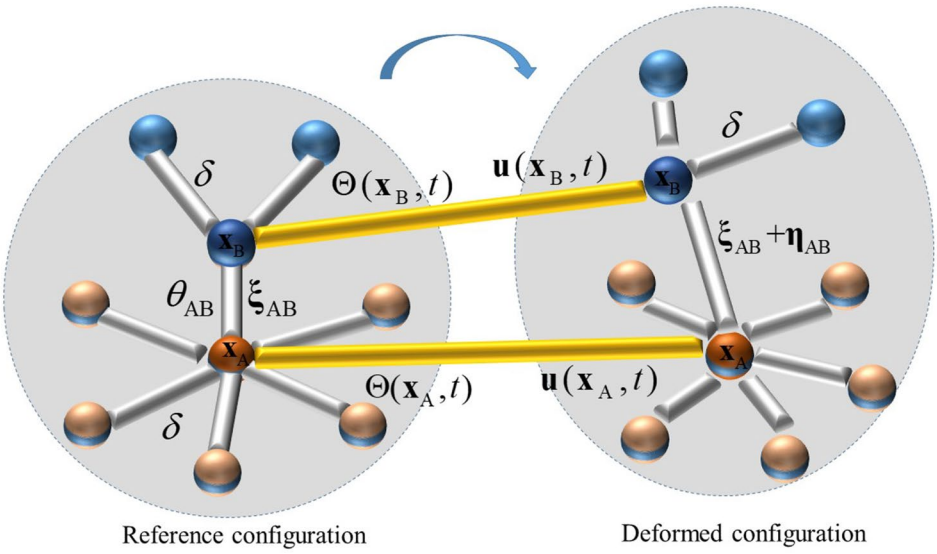

Fig. 2 Schematic diagram of the coupled thermo-mechanical bond-based peridynamics

$$f_h(\Theta_B - \Theta_A, \mathbf{x}_B - \mathbf{x}_A, t) = \kappa(\mathbf{x}_A, \mathbf{x}_B)\frac{\theta_{AB}}{|\xi_{AB}|^2}, \tag{7}$$

where $\kappa(\mathbf{x}_A, \mathbf{x}_B)$ is the micro-conductivity of the thermal bond , and is defined as

$$\kappa(\mathbf{x}_A, \mathbf{x}_B) = \frac{K(\mathbf{x}_A, \mathbf{x}_B)}{V_{H_A}}, \tag{8}$$

where V_{H_A} is the volume of the material points $\mathbf{x}_A$ with its neighboring region. $K(\mathbf{x}_A, \mathbf{x}_B)$ is the thermal conductivity of the material.

In material physics, the dislocations and slippage of the crystal ice lead to the initiation of microscopic cracks in the ice (see Fig. 3a), and the evolution of the microscopic cracks in the crystal affects the formation of macroscopic cracks (see Fig. 3b). Therefore, the macroscopic cracks are the result of the disconnection of microscopic "bonds', as shown in Fig. 3. The modeling microscopic cracks of ice in peridynamics are done by the breaking process of the "bond" between two material points. This is achieved using the bond characteristic function,

In the bond-based peridyanmics, the prototype micro-brittle (PMB) model is used to simulate the elastic and brittle mechanical responses of the material. In reality, the mechanical behavior of ice has a viscoplastic "creep" stage in the interval between elastic deformation and fracture. In this work, a "strain softening model" is used to describe the relationship between the force density function and the bond elongation, as illustrated in Fig. 4. The corresponding bond characteristic function is defined as

$$\mu_h(\xi_{AB}, \eta_{AB}, \theta_{AB}, t) = \begin{cases} 1, & s \in [0, \gamma s_0] \\ \frac{s_0 - (s - \alpha\theta_{AB})}{s_0 - \gamma s_0}, & s \in [\gamma s_0, s_0] \\ 0, & s \in [s_0, +\infty], \end{cases} \tag{9}$$

where $\gamma \in (0, 1)$ is the "strain softening factor". In the above expression, s_0 is defined as the critical stretch of the ice, which is the limit value of the longitudinal strain. The ice is deformed under the external force. As the deformation increases, the force between the material points increases with the increase in elongation until it reaches the limit. Then, the ice reaches the limit will not bear any force, and the interaction force will change to be zero.

From Fig. 4 and Eq. (9), one may find that as the deformation increases, the material first exhibits elastic deformation, and in the transition region between elastic deformation and failure, the material shows a transitional "strain softening" stage, which is equivalent to "creep" in the failure mode of ice. As the elongation of the "bond" continues to increase, the deformation of the material continues to increase, reaching the maximum strain limit, and the material will fail, and the material cannot bear any external force. With this elastic-strain softening model, we established a coupled thermo-mechanical, bond-based peridynamic, thermoelastic-strain softening ice constitutive model, which not only can simulate the elastic and brittle behavior of ice material, but also can be used to describe elastoplastic mechanical behavior of ice in the "creep" stage.

In peridynamics, the local failure index is usually used to define the unbroken bond. The failure factor index of

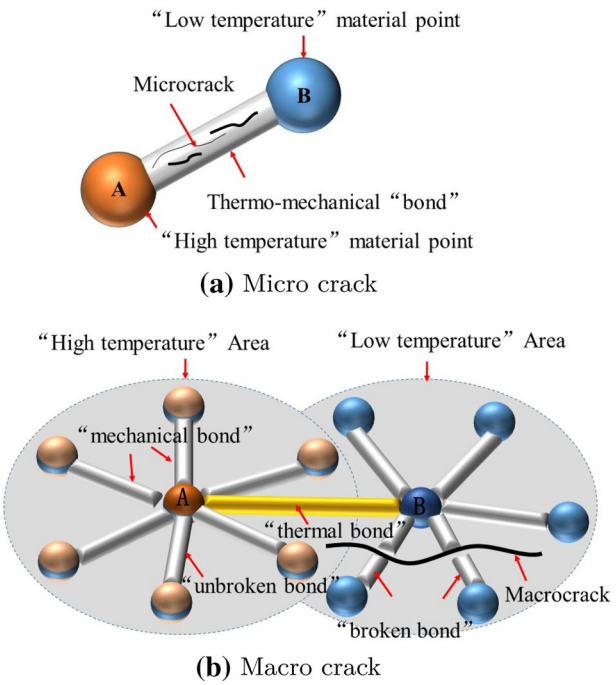

Fig. 3 Multi-scale crack in the ice

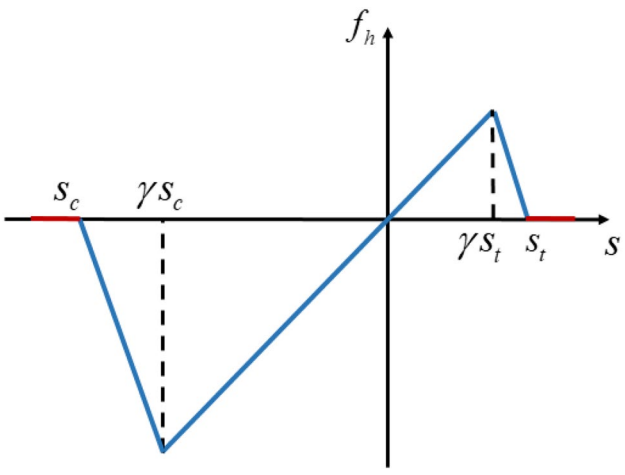

Fig. 4 The ice constitutive model in the framework of thermo-mechanical bond-based peridynamics

unbroken bond between material points can be expressed as follows:

$$\phi_h(\mathbf{x}_A, t) = 1 - \frac{\int_{H_{x_A}} \mu_h(\boldsymbol{\xi}_{AB}, \boldsymbol{\eta}_{AB}, \theta_{AB}, t) dV_{x_B}}{\int_{H_{x_A}} dV_{x_B}}. \tag{10}$$

When the microscopic "bond" $\boldsymbol{\xi}_{AB}$ breaks due to deformation beyond the critical stretch s_0, a microscopic crack is generated. This is the initiation of the initial microscopic crack. When the "bond" is broken, a crack forms and starts to grow, and the continuous growth of the crack finally produces a macroscopic crack. Under certain temperature conditions, there is heat conduction between material points, and the effect of heat conduction between material points can be simulated using "t-bond", which is the coupled peridynamic thermo-mechanical diffusion or heat conduction. The initiation and propagation of micro-cracks are determined by the mechanical bond breaking process. It is assumed that the "t-bond" is independent from the mechanical bond. When the micro-cracks occur, there is still a temperature difference and heat conduction between the material points.

The critical stretch s_0 determine when the bond will break. s_0 is related to the energy release rate G_0. The total bond energy per unit damage surface that divides the material points into two parts is the energy release rate G_0 (see Yu and Li [71]). By solving the integral equation, we can identify the critical stretch s_0 in terms of the material energy release G_0. Since the value can be obtained from the ice material, under the assumption that the damaged surface is completely separated, and there is no dissipation of other forces at the crack tip, the critical value of elongation of bond-based s_0 can be obtained as follows:

$$s_0 = \sqrt{\frac{5\pi G_0}{18E\delta}}, \tag{11}$$

where E is Young's modules of the material, and δ is the horizon.

The critical energy release rate G_0 reflects the ability of materials to resist crack propagation [56]. When the energy release rate at a material point reaches to the critical energy release rate, G_0, the crack will either initiate or grow at that material point. In the theory of linear elastic fracture mechanics, there are three crack modes: Mode I, II, and III. The formation of ice cracks is mainly the Mode I tensile failure, because the compressive strength of ice is about 3–4 times of tensile strength. The strength of ice can be characterized by the fracture toughness coefficient K_I, which is related to temperature and other parameters, and its value can be obtained from experimental studies, e.g., Dempsey [9]. The relationship between energy release rate G_0 and fracture toughness coefficient K_I can be expressed as follows:

$$G_0 = \frac{K_I^2}{E}. \tag{12}$$

The fracture toughness coefficient K_I can be used to calculate s_0, and it can be expressed as follows:

$$s_0 = \sqrt{\frac{5K_I^2}{18E^2\delta}}. \tag{13}$$

In this work, considering the thermal effects, we propose a critical stretch that depends on temperature effect, denoted as s_0^{TH}. As a new failure criterion, to improve the method based on energy rule. The purpose of the proposed failure criterion is to predict the thermo-mechanical coupling failure process of ice more accurately

$$s_0^{\mathrm{TH}} = \begin{cases} s_0 \exp\left(-\frac{\Theta - \Theta_c}{\Theta_c - \Theta_0}\right), & \Theta \geq \Theta_c \\ s_0, & \Theta \leq \Theta_c, \end{cases} \tag{14}$$

where Θ_0 represents the initial temperature of the material, Θ_c represents the critical temperature of the material, and Θ represents the ambient temperature of the material at macroscale. While at mesoscale, the local temperature difference is measured by θ_{AB}, which is the temperature difference between the material points $\mathbf{x}_A$ and $\mathbf{x}_B$. If $\Theta \geq \Theta_c$, the critical stretch function with temperature sensitivity s_0^{TH} decreases rapidly, it indicates that the ice with higher temperature is easier to break than the ice with low freezing temperature. In the calculation, the critical temperature is set to be $\Theta_c = 0\,^{\circ}\mathrm{C}$.

2.2 Thermo-mechanical boundary conditions

In this paper, the boundary conditions was imposed in ice layer as thermal heat flux.

2.2.1 Temperature condition

As shown in Fig. 5, the temperature can be prescribed in ice layer of a virtual region $\mathfrak{R}_t$ as

$$\begin{aligned} \Theta(\mathbf{y}_B^*, t^{\mathrm{TH}} + \Delta t^{\mathrm{TH}})\big|_{\mathbf{y}_B^* \in \mathfrak{R}_t} &= 2\Theta^*(\mathbf{y}_A, t^{\mathrm{TH}} + \Delta t^{\mathrm{TH}})\big|_{\mathbf{y}_A \in \Im_t} \\ &\quad - \Theta(\mathbf{y}_B, t^{\mathrm{TH}} + \Delta t^{\mathrm{TH}})\big|_{\mathbf{y}_B \in \mathfrak{R}}, \end{aligned} \tag{15}$$

where $\mathbf{y}_B$ is the position of the ice particle in the actual region $\mathfrak{R}$, $\mathbf{y}_B{}^*$ is the position of the ice particle in the virtual region $\mathfrak{R}_t$, $\mathbf{y}_A$ is the position of the ice particle on the boundary surface $\Im_t$. $\mathbf{y}_B{}^*$ is the mirror image of $\mathbf{y}_B$; see Fig. 5.

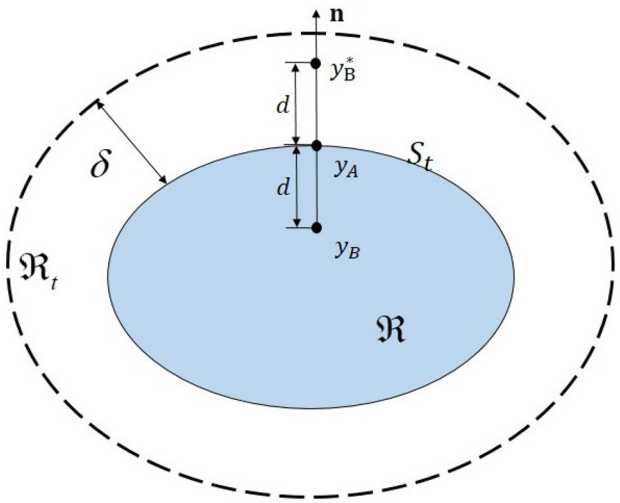

(a) Material points and its mirror image

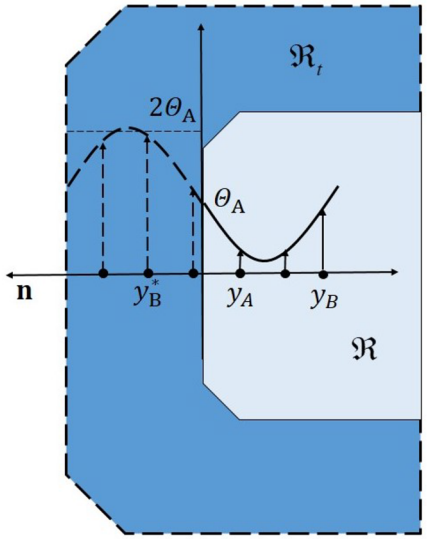

(b) Thermal condition in constant value

Fig. 5 Thermal boundary condition [55]

2.2.2 Heat flux condition

In peridynamics, heat flux $\mathbf{q}$ can be applied as the heat resource h_s over the surface $\mathfrak{T}_f$ in ice layer of the boundary region $\mathfrak{R}_f$ as follows [55]:

$$h_s = \frac{-\int_{\mathfrak{T}_q} \mathbf{q}\cdot\mathbf{n}d\mathfrak{T}}{V_f} = -\frac{\mathbf{q}\cdot\mathbf{n}}{\Delta}, \tag{16}$$

where Δ is the boundary distance, and can be taken as the horizon size δ.

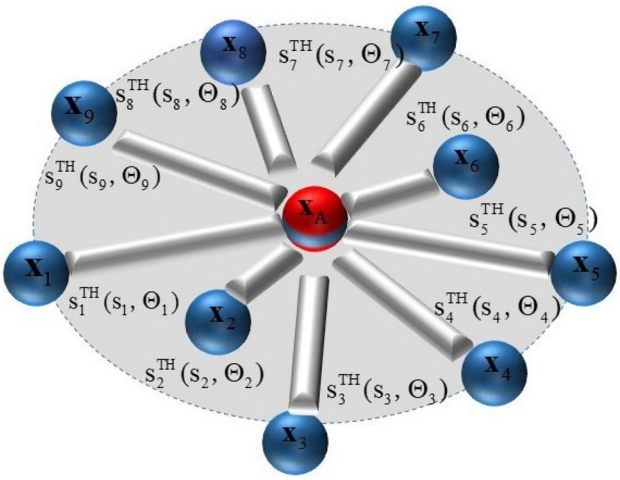

Fig. 6 The material point $\mathbf{x}_A$ and its family member with different bonds

2.3 Peridynamic model of inhomogeneous ice

In peridynamic theory, material "bond" is used to model material integrity, and the break of bonds can describe crack formation in an elastic brittle material. The break of a bond is determined by the critical stretch s_0. The critical stretch s_0 is often a constant due to the assumption that the physical properties are the same in the homogeneous material. However, sea ice is an inhomogeneous material, and its physical properties are different. Thus, the material parameters for the bond be chosen as constants if a material is inhomogenous. Thus, for inhomogeneous ice, its critical stretch s_0 is a variable.

As shown in Eq. (15), the critical stretch of the ice s_0^{TH} is influenced by the temperature. Figure 6 shows all the material points surrounding the material point $\mathbf{x}_A$ within the distance of δ, which is the radius of the horizon $H_{\mathbf{x}_A}$. For all these material points, their bonds with $\mathbf{x}_A$ have different temperatures, and hence, different critical stretches s_i, $(i = 1, 2, \ldots, n)$ and the s_0^{TH} can be determined by the following equation:

$$s_i^{\mathrm{TH}} = s_0^{\mathrm{TH}}(s_i,\Theta_i) = \begin{cases} s_i \exp\left(-\frac{\Theta_i-\Theta_c}{\Theta_c-\Theta_0}\right), & \Theta_i \geq \Theta_c \\ s_i, & \Theta_i \leq \Theta_c, \end{cases} \tag{17}$$

where Θ_i denotes the temperature at the material point $\mathbf{x}_i$, $(i = 1, 2, \ldots n)$. s_i^{TH} is the temperature-dependent critical bond stretch at the material point $\mathbf{x}_i$, $(i = 1, 2, \ldots n)$. The set of material points $\mathbf{x}_i$, $(i = 1, 2, \ldots n)$ is a family points inside the horizon H_A with the radius δ, and each material point $\mathbf{x}_i$ has different s_i and Θ_i. Comparing with Eq. (14), the critical stretch defined in Eq. (17) changes from bond to bond.

To take into account the random distributed damage, it is reasonable to think that the material damage or defect in an

ice material may obey certain probability distribution, and this may be model by assuming that the bond critical stretch s_i is a random variable.

Thus, we assumed that the critical stretch s_0 of each bond obeys the Weibull distribution function. The probability density function (PDF) can then be expressed as follows:

$$f_S\left(s_i^{\mathrm{TH}}\right)=\begin{cases}\frac{m}{\overline{s}_i^{\mathrm{TH}}}\left(\frac{s_i^{\mathrm{TH}}}{\overline{s}_i^{\mathrm{TH}}}\right)^{m-1}\exp\left[-\left(\frac{s_i^{\mathrm{TH}}}{\overline{s}_i^{\mathrm{TH}}}\right)^{m}\right], & s_i^{\mathrm{TH}}\geq 0\\ 0, & s_i^{\mathrm{TH}}<0,\end{cases} \tag{18}$$

where s_i^{TH} is the critical stretch variable, $\overline{s}_i^{\mathrm{TH}}$ is the average critical stretch, and m is the shape parameter.

Subsequently, we can write the cumulative distribution function (CDF) as follows:

$$F_S\left(s_i^{\mathrm{TH}}\right)=\begin{cases}1-\exp\left[-\left(\frac{s_i^{\mathrm{TH}}}{\overline{s}_i^{\mathrm{TH}}}\right)^{m}\right], s_i^{\mathrm{TH}}\geq 0.\\ 0, s_i^{\mathrm{TH}}<0\end{cases} \tag{19}$$

When choosing $\overline{s}_i^{\mathrm{TH}}=1.0\times10^{-3}$ and $m=2$, $m=3$, $m=4$, $m=5$, $m=6$, we plot the corresponding Weibull probability distribution function (PDF) and the thermo-mechanical coupling bond variable s_i^{TH} in Fig. 7. It can be seen from Fig. 7 that as the value of m increases, the distribution range and peak value of the Weibull probability density function increase, and the mean critical stretch will approach to the critical stretch obtained based on the material energy release .

Once we choose $\overline{s}_i^{\mathrm{TH}}$ and m, we can randomly generate the critical stretch for each material point under the Weibull distribution, which provides a nonuniform, variable spatial distribution of s_0^{TH}. Figure 8 shows several

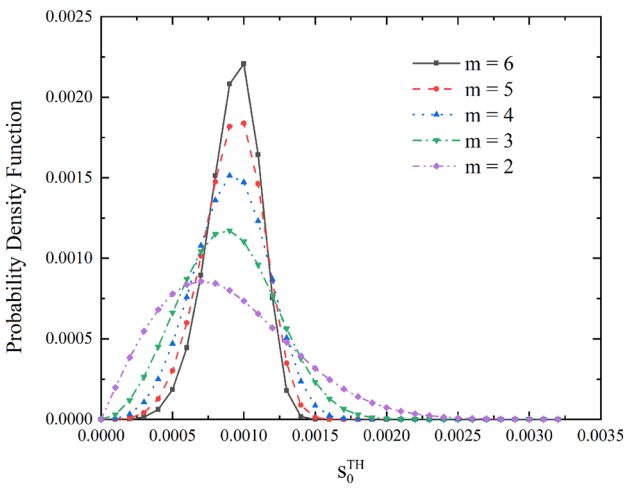

Fig. 7 The Weibull distribution function with different values of parameter m

such spatial distribution of s_0^{TH} with different values of m, which are different heterogeneous peridynamic ice models.

It can be seen more intuitively from Fig. 8 that the larger the value of m, the smaller the value of the "bond" s_i^{TH} of the material point, and the more divergent and more uniform distribution of material particles. When the value of m is infinite, the material is equivalent to a homogeneous material model.

To establish an realistic ice micro-structure model and carried out the corresponding uniaxial test, the operation steps are adopted as follows: First, we determine the distance between the particles, and then, we set the neighborhood radius as $\delta=3\Delta x$. Subsequently, we generate the Weibull distribution function to build new neighbor lists. The interaction between the particles is connected by the thermo-mechanical bond (t-bond) s_i^{TH}, and the failure of the material is determined by the break of the "t-bond" s_i^{TH}, which is controlled by the critical stretch s_0^{TH} that is related to the shape parameter m and temperature difference Θ_i. As a result, as shown in Fig. 9, the distribution of "bonds" under different grain sizes can be visually displayed. The microstructure characteristics of ice are shown in Fig. 9a–c, and the corresponding numerical model with different grain size is shown in Fig. 9d–f. From Fig. 9, we can find the distribution of the "t-bond" s_i^{TH} with different grain size Δx; the color denotes the different value of the s_i^{TH}.

2.4 Numerical procedures

In this work, the discretized equation of motion can be written as

$$\rho(\mathbf{x}_{\mathrm{A}})\ddot{\mathbf{u}}(\mathbf{x}_{\mathrm{A}},t)=\sum_{B=1}^{N}g(\boldsymbol{\xi}_{\mathrm{AB}},\boldsymbol{\eta}_{\mathrm{AB}},\theta_{\mathrm{AB}},t)\mu(\boldsymbol{\xi}_{\mathrm{AB}},\boldsymbol{\eta}_{\mathrm{AB}},\theta_{\mathrm{AB}},t)\frac{\boldsymbol{\xi}_{\mathrm{AB}}+\boldsymbol{\eta}_{\mathrm{AB}}}{\left|\boldsymbol{\xi}_{\mathrm{AB}}+\boldsymbol{\eta}_{\mathrm{AB}}\right|}\Delta V_{(\mathrm{B})}+\mathbf{b}(\mathbf{x}_{\mathrm{A}},t), \tag{20}$$

and

$$\rho(\mathbf{x}_{\mathrm{A}})c_v(\mathbf{x}_{\mathrm{A}})\dot{\Theta}(\mathbf{x}_{\mathrm{A}},t)=\sum_{B=1}^{\mathrm{N}}f_h(\Theta_{\mathrm{B}}-\Theta_{\mathrm{A}},\mathbf{x}_{\mathrm{B}}-\mathbf{x}_{\mathrm{A}},t)\mu_h(\boldsymbol{\xi}_{\mathrm{AB}},\boldsymbol{\eta}_{\mathrm{AB}},\theta_{\mathrm{AB}},t)\Delta V_{(\mathrm{B})}+h_s(\mathbf{x}_{\mathrm{A}},t), \tag{21}$$

where N is the total number of ice points that interact with $\mathbf{x}_{\mathrm{A}}$ through bonds in the horizon.

The displacement and the temperature at the $n+1$ time step can be calculated using the following time stepping algorithm:

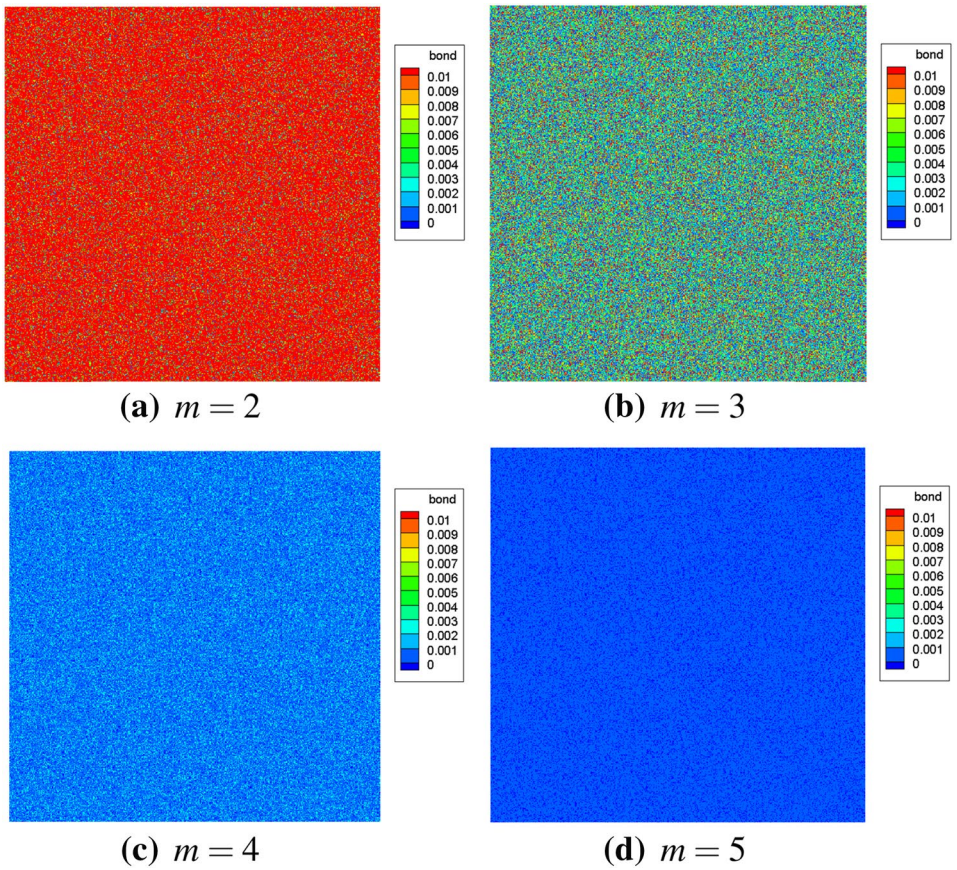

Fig. 8 Probabilistic peridynamics ice model with different values of parameter m

$$\mathbf{u}_{\mathrm{A}}^{n+1} = \mathbf{u}_{\mathrm{A}}^{n} + \frac{\Delta t}{\rho(\mathbf{x}_{\mathrm{A}})}\left\{\sum_{B=1}^{\mathrm{N}} g_{\mathrm{AB}}^{n}(\boldsymbol{\xi}_{\mathrm{AB}}, \boldsymbol{\eta}_{\mathrm{AB}}, \theta_{\mathrm{AB}}, t)\right.$$
$$\left.\mu(\boldsymbol{\xi}_{\mathrm{AB}}, \boldsymbol{\eta}_{\mathrm{AB}}, \theta_{\mathrm{AB}}, t)\frac{\boldsymbol{\xi}_{\mathrm{AB}} + \boldsymbol{\eta}_{\mathrm{AB}}}{|\boldsymbol{\xi}_{\mathrm{AB}} + \boldsymbol{\eta}_{\mathrm{AB}}|}\Delta V_{(\mathrm{B})} + \mathbf{b}^{n}(\mathbf{x}_{\mathrm{A}}, t)\right\}, \tag{22}$$

where the superscript n is the time step number, and

$$\Theta_{\mathrm{A}}^{n+1} = \Theta_{\mathrm{A}}^{n} + \frac{\Delta t^{\mathrm{TH}}}{\rho(\mathbf{x}_{\mathrm{A}})c_{v}(\mathbf{x}_{\mathrm{A}})}\left\{\sum_{B=1}^{\mathrm{N}} f_{h}^{n}(\Theta_{\mathrm{B}} - \Theta_{\mathrm{A}}, \mathbf{x}_{\mathrm{B}} - \mathbf{x}_{\mathrm{A}}, t)\right.$$
$$\left.\mu_{h}(\boldsymbol{\xi}_{\mathrm{AB}}, \boldsymbol{\eta}_{\mathrm{AB}}, \theta_{\mathrm{AB}}, t)\Delta V_{(\mathrm{B})} + h_{s}^{n}(\mathbf{x}_{\mathrm{A}}, t)\right\}. \tag{23}$$

Note that in above equations, Δt is the time step size, and Δt^{TH} is the thermal time step size.

To do so, we can finally calculate the velocity, the displacement, and the temperature at the particle point $\mathbf{x}_{\mathrm{A}}$ of the ice layer at time step $n+1$

$$\dot{\mathbf{u}}_{\mathrm{A}}^{n+1} = \ddot{\mathbf{u}}_{\mathrm{A}}^{n} + \dot{\mathbf{u}}_{\mathrm{A}}^{n}\Delta t, \tag{24}$$

$$\mathbf{u}_{\mathrm{A}}^{n+1} = \mathbf{u}_{\mathrm{A}}^{n} + \dot{\mathbf{u}}_{\mathrm{A}}^{n}\Delta t, \tag{25}$$

$$\Theta_{\mathrm{A}}^{n+1} = \Theta_{\mathrm{A}}^{n} + \Theta_{\mathrm{A}}^{n}\Delta t^{\mathrm{TH}}. \tag{26}$$

The stable time step in solving the thermo-mechanical peridynamics equations can be determined by the following criteria[54]:

$$\Delta t \leq \sqrt{\frac{2\rho(\mathbf{x}_{\mathrm{A}})}{\sum_{\mathbf{x}_{\mathrm{B}} \in H_{\mathbf{x}_{\mathrm{A}}}} \mathrm{V}_{\mathrm{B}} c(\mathbf{x}_{\mathrm{B}} - \mathbf{x}_{\mathrm{A}})}}, \tag{27}$$

and

$$\Delta t^{\mathrm{TH}} \leq \frac{\rho(\mathbf{x}_{\mathrm{A}})c_{v}(\mathbf{x}_{\mathrm{A}})}{\sum_{j=1}^{N} \frac{\kappa}{|\xi|^{2}} \mathrm{V}_{x_{j}}}. \tag{28}$$

An adaptive dynamic relaxation method is adopted in this simulation; according to the study by Kilic [20], the adaptive dynamic relaxation method is applicable in nonlinear peridynamic equations.

A flowchart of the numerical procedure is shown in Fig. 10.

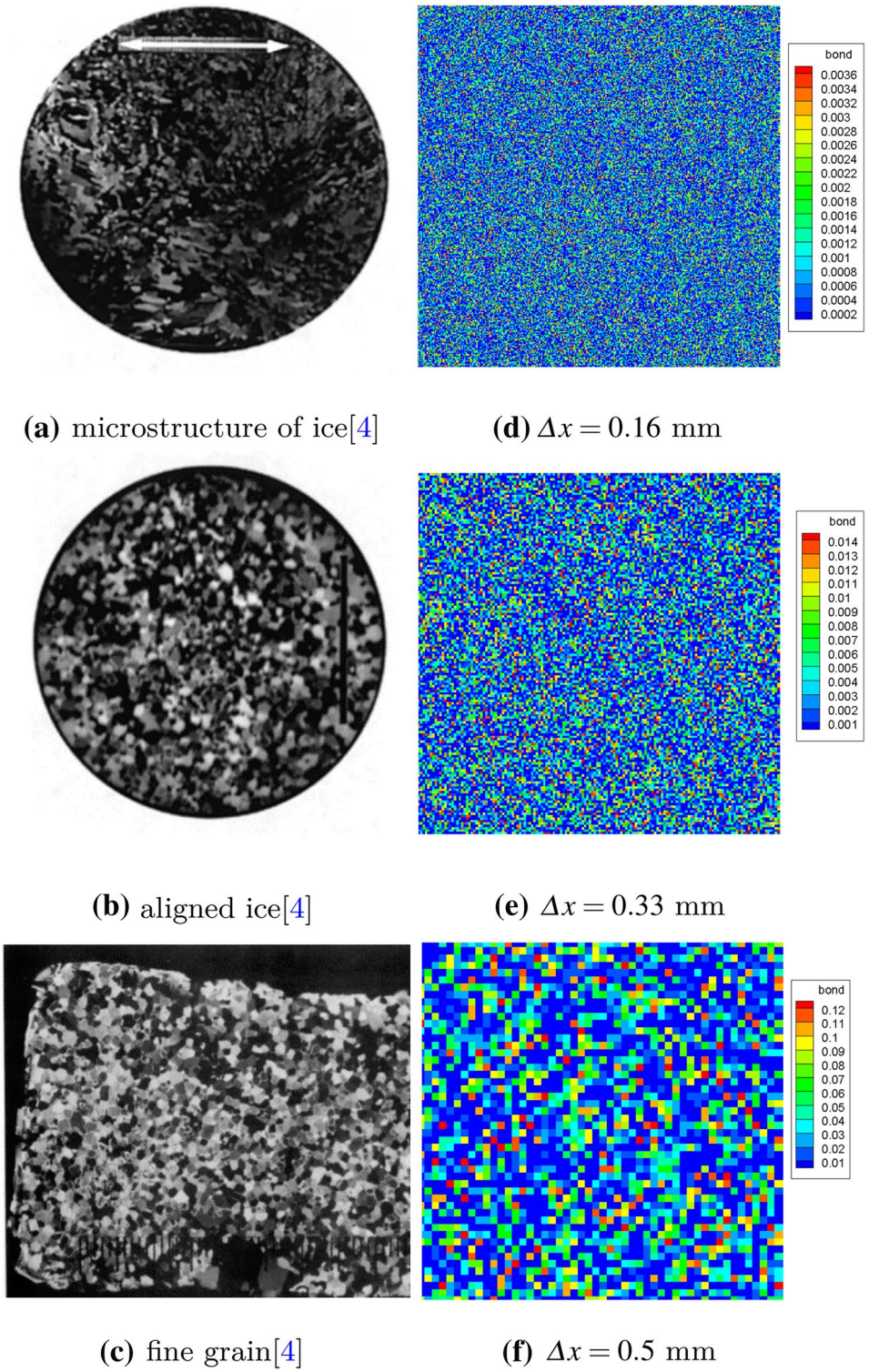

Fig. 9 Inhomogeneous ice models with different grain sizes: (**a**) microstructure of ice [4] (**b**) aligned ice [4] (**c**) fine grain [4].

3 Numerical examples

The formation process of ice has undergone internal changes, especially for multi-year ice, which is affected by the flow field of water and air in nature, or the collision, polishing, and transformation of rocks and other external bodies, so that various textures and impurities are formed inside, and many initial defects. These initial defects affect the mechanical properties of ice. In this section, the effect of the initial defects, temperature is studied based on the proposed nonhomogeneous ice model.

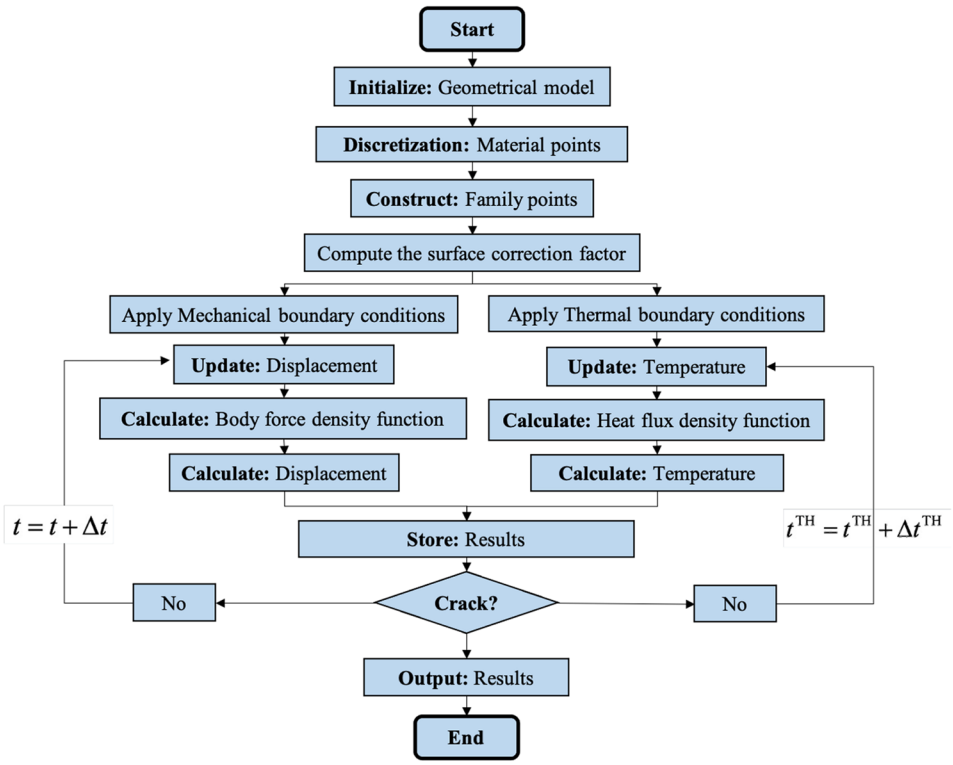

Fig. 10 Flowchart of thermal-mechanical peridynamics simulations of crack growth in ice

3.1 Wing crack failure

The "Wing-shaped" cracks can be formed on freshwater ice, saltwater ice, and granular ice. It is a main deformation characteristic of ice under high strain rate deformation. "Wing-shaped" cracks mainly exist on ice plates with initial crack defects. To verify the proposed nonhomogeneous ice model, the numerical models of ice with initial defects are based on the research reported by Schulson [49], as is shown in Fig. 11. The ice plate is subjected to a compressive load. $2a$ represents the length of the initial crack and β is the angle of the crack. The rectangular ice plate with a single preformed crack is chosen to be $2a = 0.05$ m, $\beta = 45°$, as shown in Fig.11a; four preformed cracks $2a = 0.025$ m, $\beta = 45°$, and the compressive load is chosen to be 6 MPa. The corresponding peridynamic heterogeneous discrete model is shown in Fig. 11b, d. According to the research reported in the literature, the ice material may experience a ductile-to-brittle transition during the failure process, and in this process, the ice grain size plays a major role. Generally, the diameter of ice crystal grains is in the range of 0.001–0.010 m. Based on these requirements, the ice model size is set to be 0.40 m × 0.20 m; the total number of ice particles is 80,000; the grid size is taken as $\Delta x = 0.001$ m, and the neighborhood radius is taken as $\delta = 3.015\Delta x$. Using an adaptive dynamic relaxation approach [20], we choose $\Delta t = 1$ s, and the total number of the calculation time steps is 1000 steps. The material properties of the ice are given in Table 1.

The initial conditions are

$$u_x(x, y, t = 0) = u_y(x, y, t = 0) = 0, \tag{29}$$

$$\Theta_0(x, y, t = 0) = -25\,°\text{C}. \tag{30}$$

The boundary conditions are

$$u_x(x = \pm L/2, y, t) = u_y(x = \pm L/2, y, t) = 0, \tag{31}$$

$$v_x(x = \pm L/2, y, t) = v_y(x = \pm L/2, y, t) = 0, \tag{32}$$

$$\sigma_{yy}(x, y = \pm L/2, t) = \pm 6\,\text{MPa}, \tag{33}$$

$$\Theta_x(x = \pm L/2, y, t) = 0°\text{C}, \tag{34}$$

$$\Theta_y(x = \pm L/2, y, t) = 0°\text{C}. \tag{35}$$

The comparison between numerical calculation results and experimental observation results is shown in Fig. 12. It can be seen from Fig. 12 that the calculation method in this paper can simulate the "Wing-shaped" crack of the ice plate under the compressive load. The formation of the wing-shaped crack obtained by the numerical calculation results

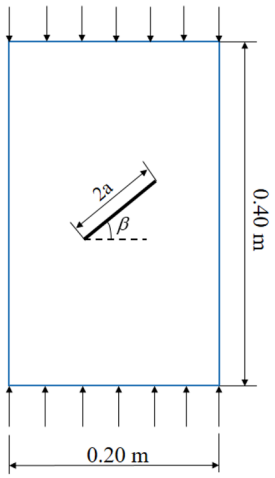

(a) Geometrical model (single pre-crack)

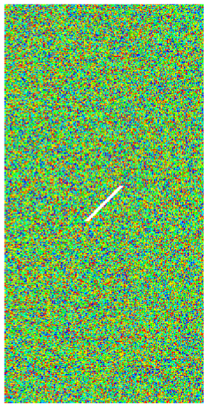

(b) Ice non-homogenous model(Single pre-crack)

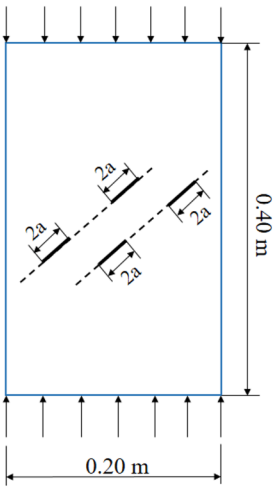

(c) Geometrical model (multiple pre-crack)

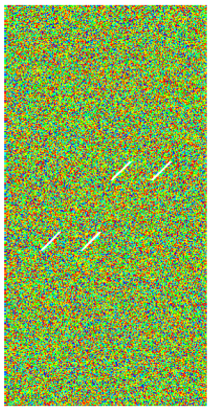

(d) Ice non-homogenous model(Multiple pre-crack)

Fig. 11 Sketch map of the ice plate with pre-existing flaw crack under the compression load

Table 1 Parameters in numerical model

Parameters	Unit	Ice
Youngs modulus E	GPa	9.31
Poisson's ratio υ	–	1/3
Density ρ	kg/m^3	897
Specific heat capacity C_v	J/kg °C	2030
Fracture toughness K_I	J/m^2	134
Thermal conductivity k	W/(m °C)	2.13
Thermal expansion coefficient α	$\times 10^{-6}$/°C	46.0

in this paper is consistent with the results of the experiment. In essence, "Wing-shaped" cracks are caused by local tensile deformation, due to possible ice crystal slip and dislocations. The "Wing-shaped" crack initiates at the crack tip, as shown in Fig. 12. The "Wing-shaped" crack initiating at the crack tip starts from the direction perpendicular to the maximum local tensile stress and expands to the maximum compressive stress direction. Another remarkable feature of crack growth is that the growth rate of "Wing-shaped" cracks at the free boundary is faster than the growth of wing-shaped cracks inside the structure. The characteristics of crack growth simulated by this paper are completely consistent with the conclusions of the experimental study by Schulson [49]. It can be seen from Fig. 12 that according to the deformation of the ice material, at the microscopic level, it is considered to be the deformation of the "bonds" between the ice particles, and the microcrack propagation process in ice can be categorized into four stages: (1) elastic deformation stage (the destruction factor is $0 \le \varphi \le 0.25$, indicated by the blue particles in the figure). The deformation of the material is linear and meets the elasticity law without cracks; (2) the elastoplastic deformation stage (destruction factor $0.25 \le \varphi \le 0.5$, indicated by the green particles). In the elastoplastic deformation stage, the deformation energy of the ice material is less than the internal energy of the material, and the material is in the elastoplastic stage without failure or failure; (3) the viscoelastic–plastic deformation stage (the failure factor is $0.5 \le \varphi \le 0.75$, indicated by the yellow particles); (4) fracture deformation stage (damage factor $\varphi \ge 0.8$, indicated by the red particles). In this stage, the macroscale crack initiates and grows steadily.

The growth process of a single pre-crack is shown in Fig. 13. "Wing-shaped" cracks are initiated from the tip of the pre-set crack and grow along the loading direction. The expansion process of multiple pre-cracked ice plates under compressive load is shown in Fig. 14. It can be seen from Fig. 14 that the cracks initially originated at the tip of the ice plate defect. At the 300th time step, a connection occurs between the adjacent pre-cracks.

The macroscopic crack propagation in ice can be defined as three stages. The first stage, i.e., the dynamic crack propagation stage. In the first stage, at the crack tip of the initial notch the ice is affected by tension and shear. The greater the amplitude of the load, the faster the crack grows. In the second stage, the stress wave "accumulates" at crack tip. The crack propagation causes the stress wave to propagate from the crack surface to the interior of the ice. The Rayleigh wave on the crack surface acts on the material points near the surface, causing the rotation of the velocity vector. When the load, along with the strain energy flux, reaches a certain value, the stress wave is generated at the crack tip at a faster speed and concentrated on the crack tip, and the stress wave is reflected and deflected at a certain angle, so

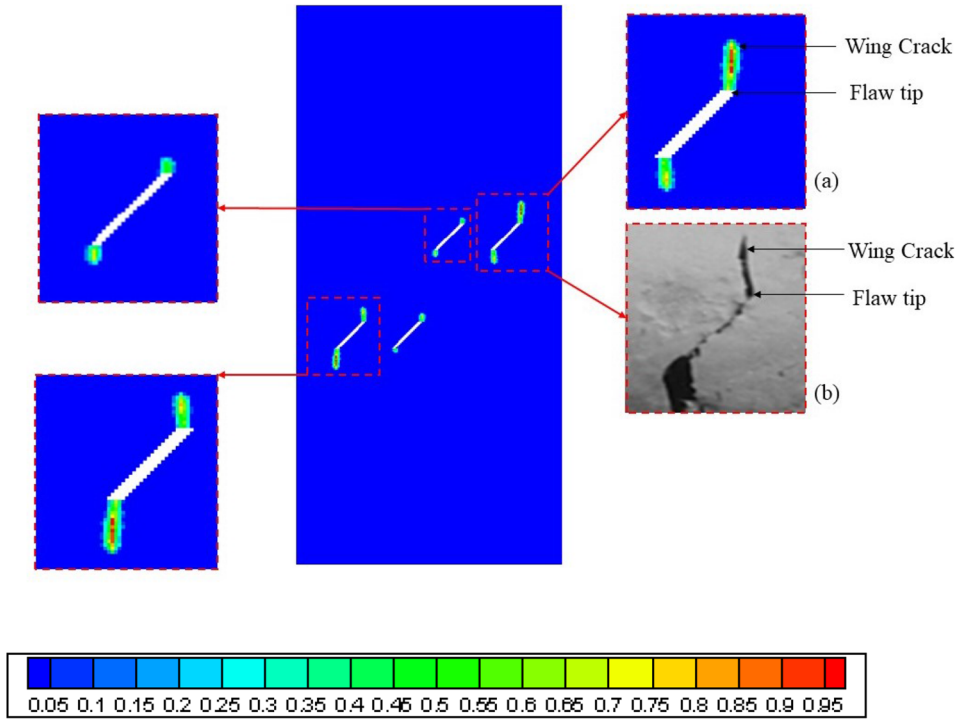

Fig. 12 W-crack under the compressive pressure: **a** results in the present study; **b** experimental data (From Schulson et al. [49])

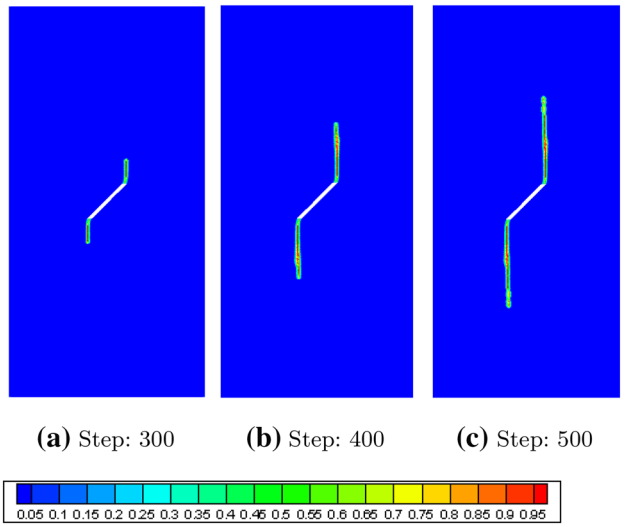

Fig. 13 The crack pattern of the ice plate with single pre-existing flaw crack under the compression load

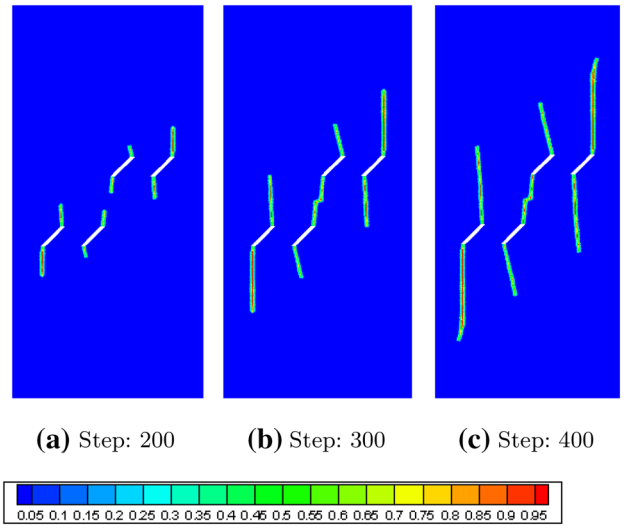

Fig. 14 The crack pattern of the ice plate with multiple pre-existing flaw crack under the compression load

that the bond perpendicular to the crack tip, which is different from the initial defect direction, may exceed the critical stretch. The third stage, i.e., the stage of crack bifurcation and material fragmentation. In this stage, when the deformation of the "bond" exceeds the critical stretch, the "bond" breaks, and the broken bond causes the cracks start to grow and propagate.

To discuss the influence of the initial flaw angle of the "W" crack. The numerical ice layer used in the simulation has the dimension of 0.05 m × 0.05 m, $2a = 0.025$ m, $\beta = 0°$, $\beta = 15°$, $\beta = 30°$, $\beta = 45°$, $\beta = 60°$, $\beta = 75°$, $\beta = 90°$, respectively. The material properties are similar with the previous study, as is shown in Table 1. The total number of discrete particles is 250,000. The grid size is taken as $\Delta x = 0.0001$ m, and the neighborhood radius is taken as $\delta = 3.015\Delta x$. The dynamic relaxation technology is being used, the time step size is chosen to be $\Delta t = 1$ s, and the total calculation time is 1000 steps. The initial conditions

are $\Theta_0(x, y, t = 0) = -20\,^{\circ}\mathrm{C}$, $\Theta_0(x, y, t = 0) = -10\,^{\circ}\mathrm{C}$, $\Theta_0(x, y, t = 0) = -6\,^{\circ}\mathrm{C}$, $\Theta_0(x, y, t = 0) = -4\,^{\circ}\mathrm{C}$, respectively.

The boundary conditions are

$$\sigma_{yy}(x, y = \pm L/2, t) = \pm 6\,\mathrm{MPa}, \tag{36}$$

$$\Theta_x(x = \pm L/2, y, t) = 0\,^{\circ}\mathrm{C}, \tag{37}$$

$$\Theta_y(x = \pm L/2, y, t) = 0\,^{\circ}\mathrm{C}. \tag{38}$$

The comparison of calculation results under different pre-crack angles and different temperature conditions are shown in Fig. 15. It can be seen from Fig. 15 that the angles of crack initiation and propagation are all along the direction of loading stress. The crack propagation forms at different initial ice temperatures are the same, but the crack area is slightly different. The higher the initial ice temperature, the larger the expanded crack area is. The initial temperature of ice affects the strength, and the strength of ice decreases with the increase of temperature. When the initial defect crack angle is $\beta = 0°$, the shape of the branch is similar to "H" type crack, and it is formed as "I" type crack when the initial flaw angle is $\beta = 90°$. When the initial defect crack angle is $\beta = 15°$–$75°$, "W"-shaped crack appears.

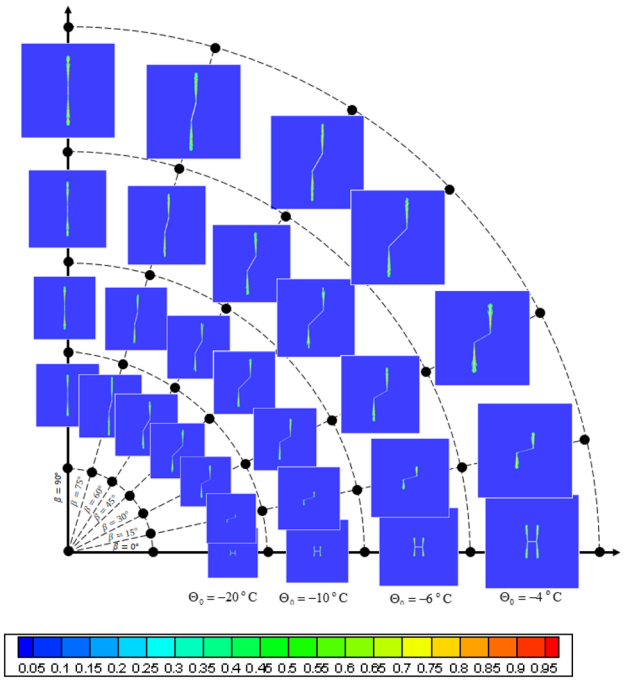

Fig. 15 Crack patterns at different pre-crack angle and different initial temperature conditions

3.2 Uniaxial tensile failure of ice with different initial flaw

To analyze the crack propagation process and crack formation of nonhomogeneous ice, and explain the mechanism of the initiation and propagation of the crack in the sea ice plate with initial defect. We present several sea ice models with different initial defects. The initial defect of rhombus, square, longitudinal rectangle, and transverse rectangle are, respectively, selected. The geometric model is chosen to be $x = y = 0.05$ m, and the specific initial defect hole size is as follows: $x = y = 0.01$ m in rhombus model; $x = y = 0.01$ m in square model; $x = 0.005$ m, $y = 0.01$ m in longitudinal rectangle model, and $x = 0.01$ m, $y = 0.005$ m in transverse rectangle model, as is shown in Fig. 16. The ice plate under the action of tensile load on the top and bottom of the ice plate, and the tensile stress value is 0.1 MPa. The ice plate is discretized into 250,000 particles, using adaptive dynamic relaxation technology, $t = 1$ s. The total calculation time is 1000 steps.

Initial conditions are

$$u_x(x, y, t = 0) = u_y(x, y, t = 0) = 0, \tag{39}$$

$$\Theta_0(x, y, t = 0) = -25\,^{\circ}\mathrm{C}. \tag{40}$$

Boundary conditions

Case 1:

$$\sigma_{yy}(x, y = \pm L/2, t) = \pm 0.1\,\mathrm{MPa}. \tag{41}$$

Case 2:

$$\sigma_{yy}(x, y = \pm L/2, t) = \pm 0.1\,\mathrm{MPa}, \tag{42}$$

$$\Theta_x(x = \pm L/2, y, t) = 0\,^{\circ}\mathrm{C}, \tag{43}$$

$$\Theta_y(x = \pm L/2, y, t) = 0\,^{\circ}\mathrm{C}. \tag{44}$$

Figure 17a, c, e, g shows the result of the crack propagation form in case 1, and Fig. 17b, d, f, h shows the result of the ice cracking form in case 2.

It can be seen from Fig. 17a, c, e, g that under the single stress load, the crack form of the ice plate with the initial defect is a radial crack. The crack starts from the tips of the defect, then grows laterally along the mechanical loading direction, and there is no bifurcation crack. One may also find from Fig. 17b, d, f, h that under the coupled thermo-mechanical load, the crack initiates from the tip and grows horizontally and longitudinally. When the crack expands to a certain range, bifurcation begins to appear.

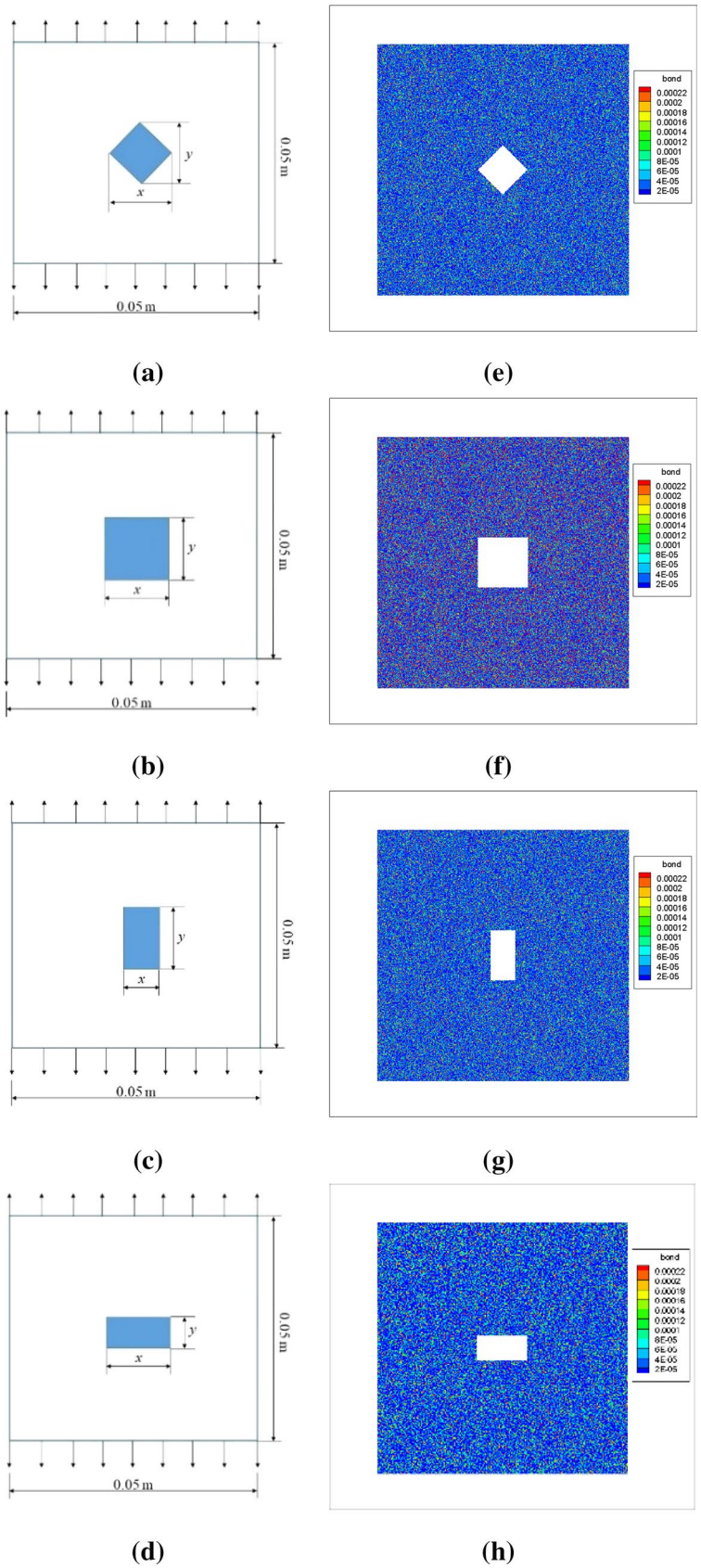

Fig. 16 The ice model with a pre-existing flaw: geometrical model (**a**–**d**); nonhomogenous model (**e**–**h**)

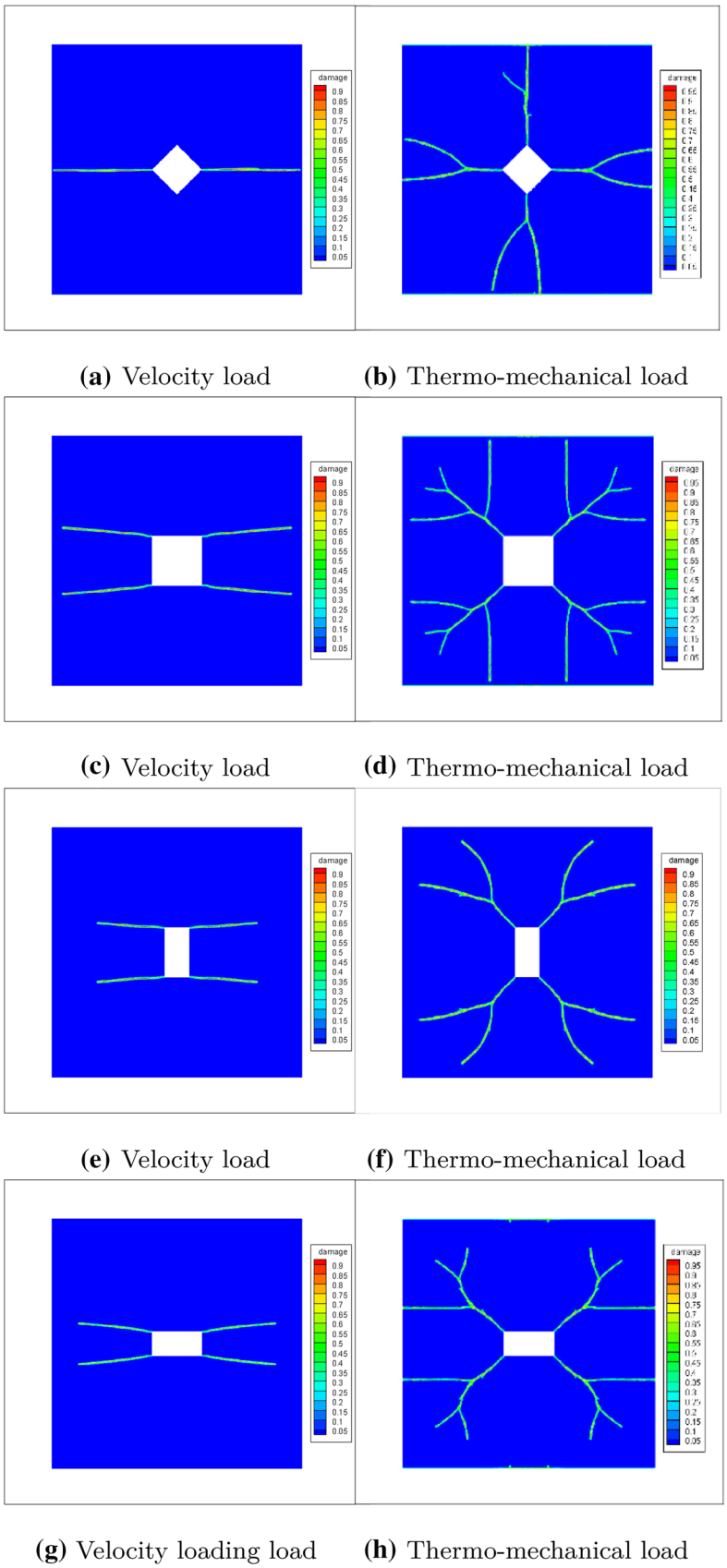

(a) Velocity load **(b)** Thermo-mechanical load

(c) Velocity load **(d)** Thermo-mechanical load

(e) Velocity load **(f)** Thermo-mechanical load

(g) Velocity loading load **(h)** Thermo-mechanical load

Fig. 17 Comparison between the crack pattern in the ice plate with different pre-existing flaw

Such crack form and crack propagation process of sea ice are more close to the realistically.

3.3 Crack in ice containing bubbles

After the sea water freezes into ice, crystals are formed, causing voids in the ice. At the same time, the gas dissolved in the water is forced out to form tiny bubbles, which makes the density of the ice smaller and larger than the original water, and the water freezes. When the water freezes, the gas can no longer be dissolved by the ice, it will slowly reduce to gas during the freezing process, and become many small bubbles. To simulate the crack in the ice with bubbles, several sea ice numerical models with random pores are taken in this study, and the relationship between porosity and failure strength is discussed.

3.3.1 Numerical model

In this study, the geometrical model is shown in Fig. 18a, the radius of the initial round pore hole is R, and the pore hole diameter is chosen to be $R = 0.001$–0.015 m, respectively. Vertical pulling force is applied on the boundary between the top and bottom of the plate. The established numerical models based on the peridynamics are shown in Fig. 18b–e. It can be seen from Fig. 18b–e that the uniformity of the material is affected by the shape parameter m. As the value of m increases, the value of the material bond gradually decreases, which tends to be a homogeneous material. In this simulation, the particle dispersion rate is chosen to be $m = 4$. The particle distance is chosen to be $\Delta x = 0.1$ mm. The ice plate is discretized into 250,000 particles, using adaptive dynamic relaxation approach, $t = 1$ s. The total calculation time is 1000 steps.

Initial conditions are

$$u_x(x, y, t = 0) = u_y(x, y, t = 0) = 0, \tag{45}$$

$$\Theta_0(x, y, t = 0) = -25 \text{ to } -4\,^{\circ}\text{C}. \tag{46}$$

Boundary conditions

Case 1:

$$\sigma_{yy}(x, y = \pm L/2, t) = \pm 0.01\ \text{MPa}, \tag{47}$$

$$\Theta_x(x = \pm L/2, y, t) = 0\,^{\circ}\text{C}, \tag{48}$$

$$\Theta_y(x = \pm L/2, y, t) = 0\,^{\circ}\text{C}. \tag{49}$$

Case 2:

$$\sigma_{yy}(x, y = \pm L/2, t) = \pm 0.02\ \text{MPa}, \tag{50}$$

$$\Theta_x(x = \pm L/2, y, t) = 0\,^{\circ}\text{C}, \tag{51}$$

$$\Theta_y(x = \pm L/2, y, t) = 0\,^{\circ}\text{C}. \tag{52}$$

In this work, the simulation is conducted with a number of threats 64(N) in a CPU model of Intel(R)Core(TM) i7-8700U CPU, of main frequency 3.20 GHz. The Fortran 90 code is compiled using the Intel Parallel Studio XE 2012. The total simulation time is around 0.5 h. We first compared the uniform mesh and the nonuniform mesh, respectively. The comparison results are shown in Fig. 19. It can be seen from Fig. 19 that it is more prone to reveal cracks using the nonuniform mesh.

3.3.2 Mechanism of crack formation in ice containing bubbles

The crack shape of the ice plate under the thermo-mechanical coupling loading condition is shown in Figs. 20, 21, 22 and 23.

It can be seen from Figs. 20, 21, 22 and 23 that the temperature difference is the main influencing factor of the crack shape, and the temperature difference leads to the bifurcation of the crack. Under the mechanical loading conditions, the ice plate is dominated by type I cracks. However, under the thermo-mechanical coupling loading condition, the ice plate has type II bifurcation cracks. The greater the temperature difference, the more cracks will branch, and the higher the initial temperature, the earlier the crack arrest time will be. Besides, the crack growth is affected by the heat flux, it expands linearly without considering the heat flux, and branching and expansion occurs under the action of the heat flux. Under coupled thermo-mechanical conditions, the stress concentration phenomenon of the velocity field occurs during the wave propagation in the ice medium, which is the internal mechanical mechanism of crack bifurcation and propagation.

Figure 24 shows the average elastic wave velocity of an ice plate with pre-crack before crack propagation occurs. From Fig. 24, we can find that the calculation results in this work are basically consistent with the changes in the wave velocity measured by the experiment [24]. The wave propagation velocity decreases with the increase of the initial ice temperature; under the same temperature condition, the transverse wave speed is about 1.6 times that of the longitudinal wave, the transverse wave speed is about 400–1400 m/s, and the longitudinal wave speed is about 800–2100 m/s.

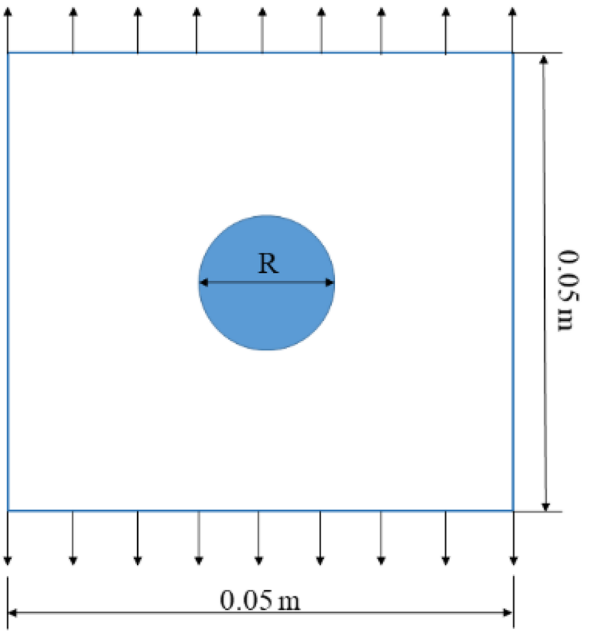

(a) geometrical model

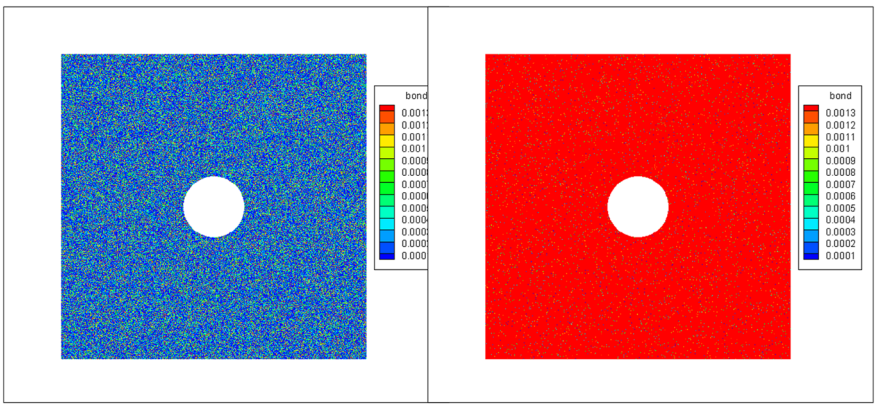

(b) ice model $m = 4$ (c) ice model $m = 2$

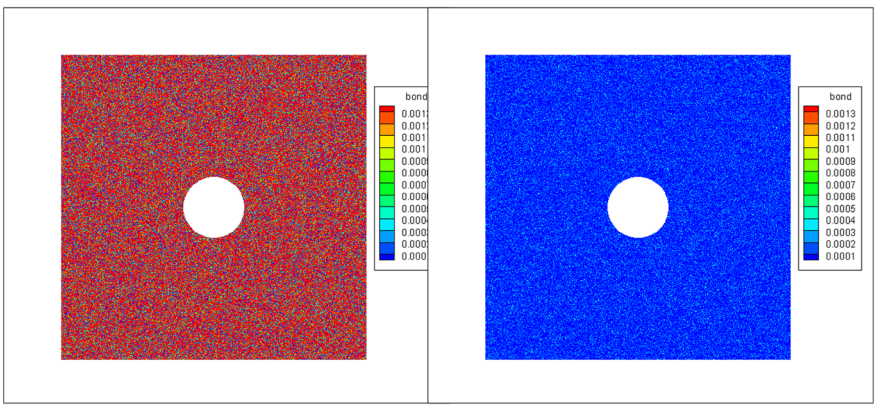

(d) ice model $m = 3$ (e) ice model $m = 5$

Fig. 18 The ice model with a pre-existing hole under the tensile velocity condition

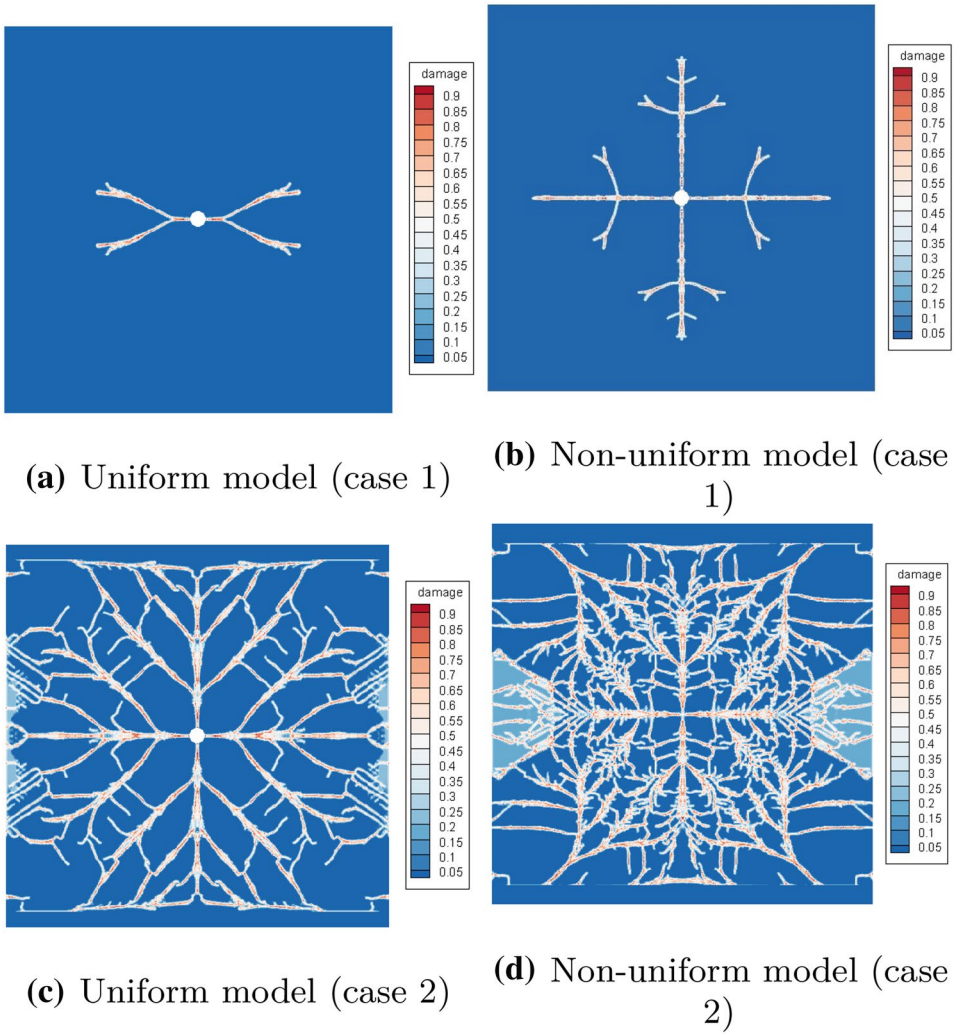

Fig. 19 Comparison of ice cracking between the uniform mesh and the nonuniform mesh

Figure 25 shows the crack propagation process under case 1. The damage index range is 0.05–0.90, the blue area represents the undamaged area, the red area represents the area with 90 percent damage index, and the corresponding velocity cloud diagram are shown in Fig. 26. In Fig. 26, the right part shows the velocity vector diagram of the node near the crack tip, corresponding to the speed vector magnified cloud diagram in the red dashed box, explains the crack based on the velocity vector curve reasons for initiation, expansion, and bifurcation. The length of the velocity vector is proportional to the velocity of the corresponding node. The direction of the velocity vector represents the direction of the velocity. The blue arrow is negative, and the red arrow is positive.

Figure 26 shows the distribution of the velocity field at the corresponding crack tip. It can be seen from the figure in the red dashed box that there are opposite velocities in the positive and negative directions along the crack line in the crack tip area, and then, surface separation or cleavage appears, and the difference between positive and negative particle velocities lead to the fracture of the ice material. Figure 26 further reveals the evolution process of the velocity vector. When the ice plate is subjected to the loading force, the wave propagation starts immediately. On two sides of the crack surface, the velocity vector directions are opposite (see square area), the opposite velocity direction causes the initial cracks to grow on the surface of the material. In the area far from the crack tip,

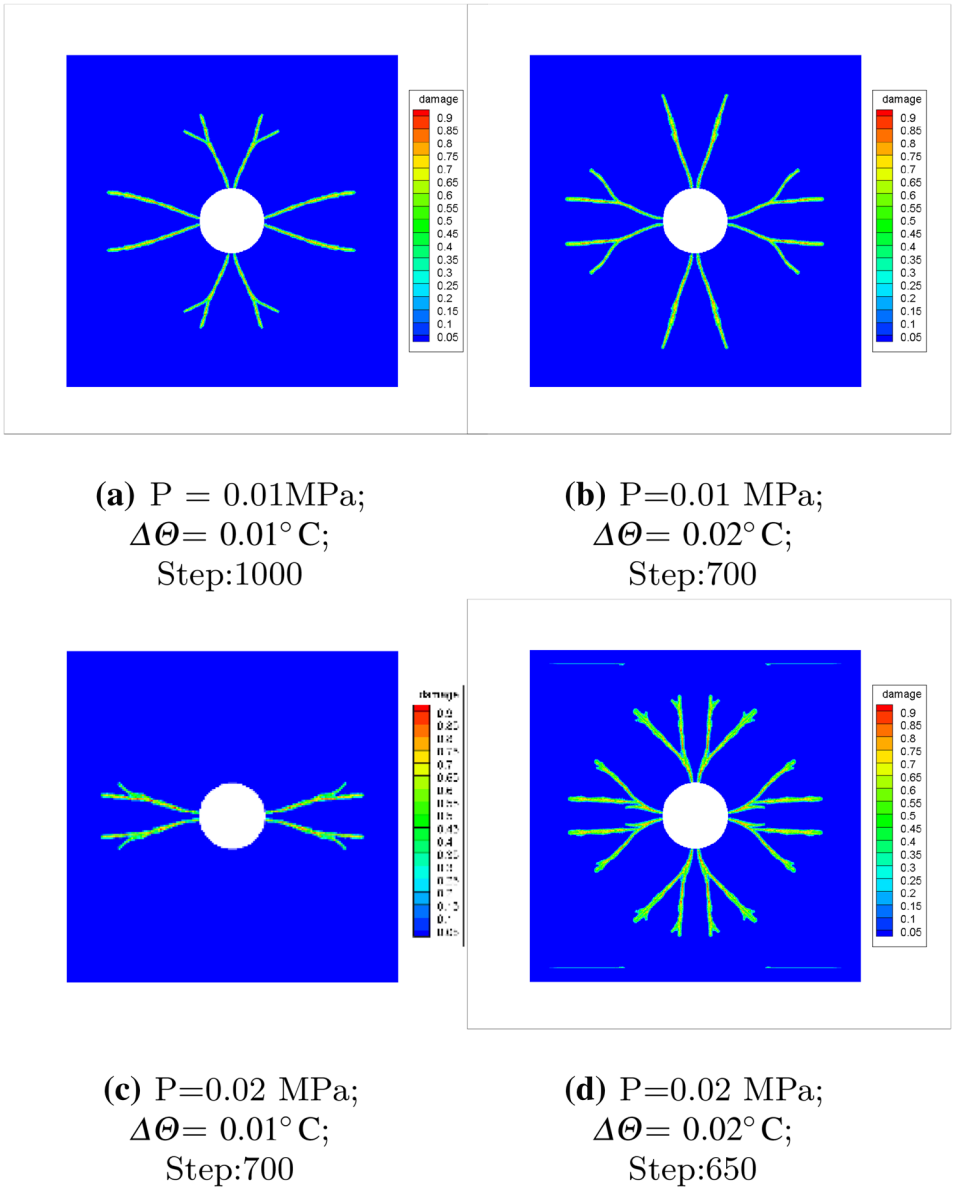

(a) P = 0.01MPa; $\Delta\Theta$= 0.01° C; Step:1000

(b) P=0.01 MPa; $\Delta\Theta$= 0.02° C; Step:700

(c) P=0.02 MPa; $\Delta\Theta$= 0.01° C; Step:700

(d) P=0.02 MPa; $\Delta\Theta$= 0.02° C; Step:650

Fig. 20 Crack patterns at different thermo-mechanical conditions $\Theta_0 = -20\,^{\circ}\mathrm{C}$

there are small vortices (inner circular areas) with material point velocity close to zero. As the cracks grow, the above area changes its position, trying to reach a steady state. Surface waves accumulate at the crack tip, and the wave propagates faster on the surface of the crack. When the bond between two material points is broken, the wave is scattered from it. In the early stage of crack propagation, when the strain energy is low, the material enters a steady state, and the crack expands directly without branching. When the strain energy accumulates to a certain value, the speed difference causes the deformation along the bonds that are perpendicular to the original crack line to exceed the critical elongation. At this time, the strain energy is released, and the crack branching process occurs. As the crack branch continues to grow, the strain energy continues to accumulate. When the wave generated by the fracture process reaches a higher amplitude, the second branch of the crack occurs. When the fracture occurs, the material relaxes, so the strain energy at the crack bifurcation tip is released.

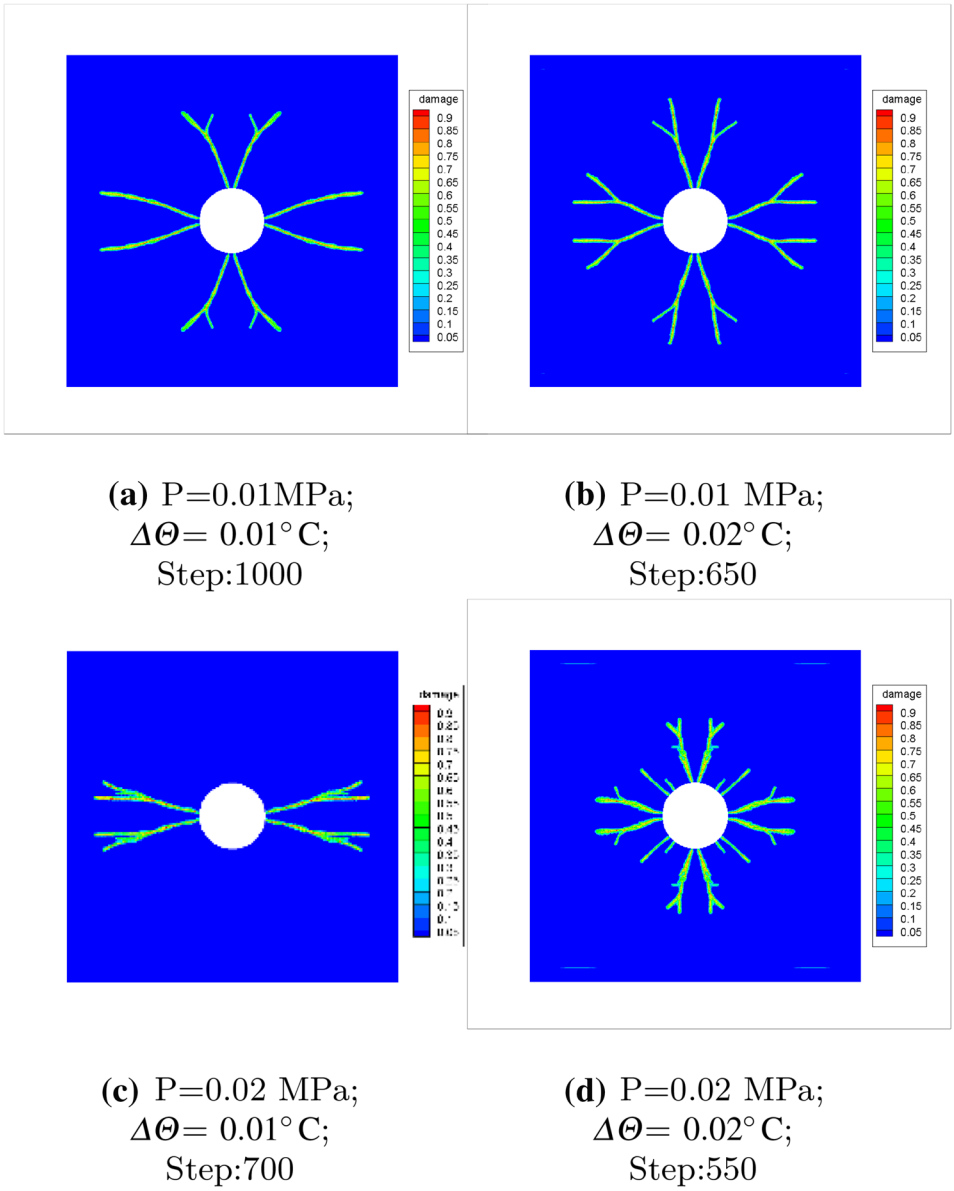

Fig. 21 Crack patterns at different thermo-mechanical conditions $\Theta_0 = -10\,^{\circ}\mathrm{C}$

3.3.3 Crack in ice containing random bubble pore

To further study the formation of the crack in ice with multiple bubble defects, and demonstrate the accuracy of our numerical model. The crack shape of an ice plate with multiple bubbles is studied using experimental method and numerical method. In the experimental test, we made the ice samples in the refrigerator, and keep the temperature in −18 °C. The experimental specimen is shown in Fig. 27.

The experimental ice plate and the numerical ice layer have the same dimension of 0.1 m × 0.1 m. The material properties are the same as Table 1. The ice plate is discretized into 250,000 particles, using the adaptive dynamic relaxation approach, $t = 1$ s. The total calculation time is 1000 steps. In this work, the simulation is conducted with a number of threats 64(N) in a CPU model of Intel(R) Core(TM) i7-8700U CPU, of main frequency 3.20 GHz. The fortran 90 code is compiled using the Intel Parallel Studio XE 2012. The total simulation time is around 0.5 h.

The initial conditions are given as follows:

$$u_x(x, y, t = 0) = u_y(x, y, t = 0) = 0, \tag{53}$$

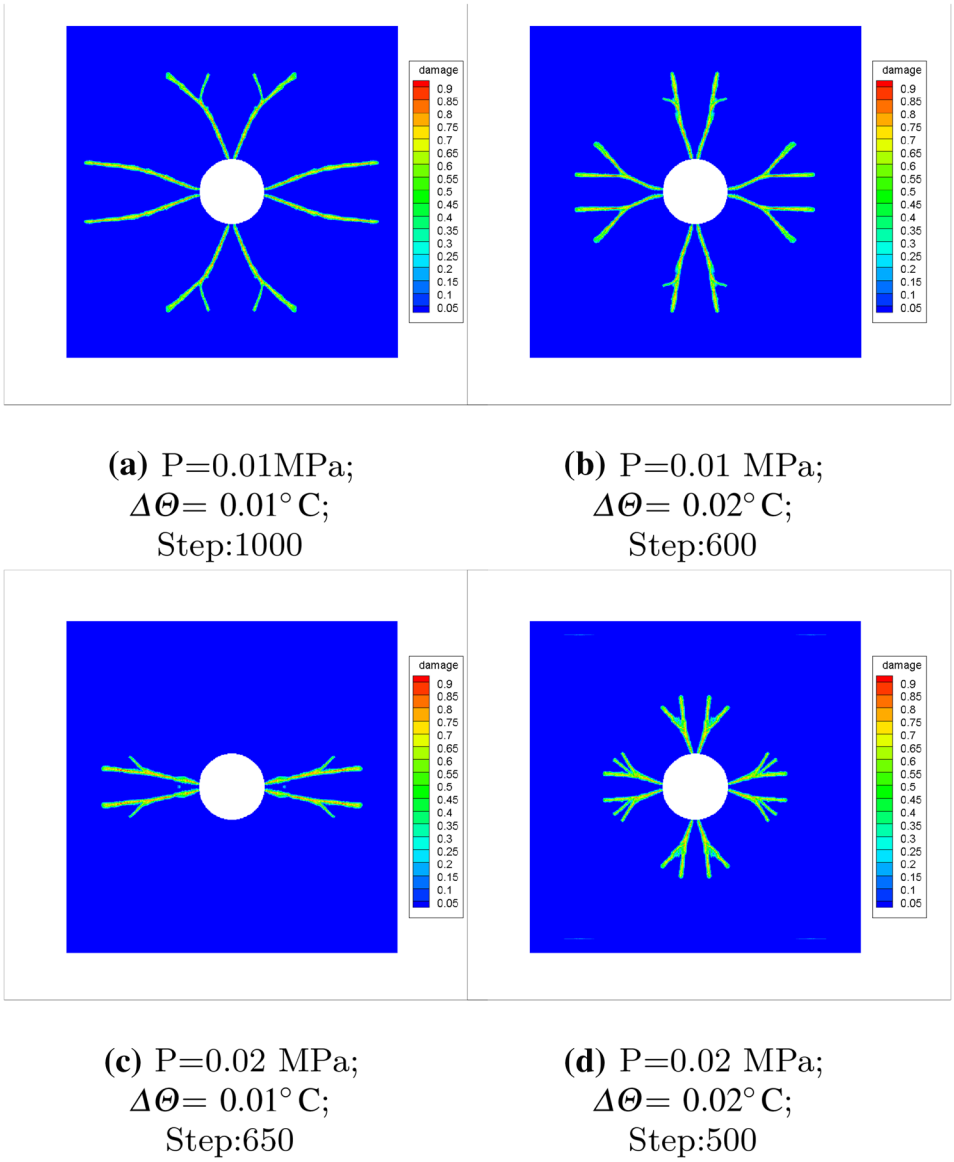

Fig. 22 Crack patterns at different thermo-mechanical conditions $\Theta_0 = -6\,^{\circ}\mathrm{C}$

$$\Theta_0(x, y, t = 0) = -18\,^{\circ}\mathrm{C}. \tag{54}$$

The boundary conditions are given as follows:

$$\sigma_{yy}(x, y = \pm L/2, t) = \pm 6\,\mathrm{MPa}, \tag{55}$$

$$\Theta_x(x = \pm L/2, y, t) = 0\,^{\circ}\mathrm{C}, \tag{56}$$

$$\Theta_y(x = \pm L/2, y, t) = 0\,^{\circ}\mathrm{C}. \tag{57}$$

Comparison of crack pattern in the multi-bubble ice plate is shown in Fig. 28. From Fig. 28, one can find that the simulation results obtained from peridynamics computation are consistent with the experimental result. Due to the mutual influence between the bubble holes, the cracks show irregular expansion, and type I cracks and type II cracks appear at the same time, and the cracks between similar bubble holes appear cross-fusion. These results indicate that the calculation method in this paper can simulate the process of crack initiation, crack propagation,

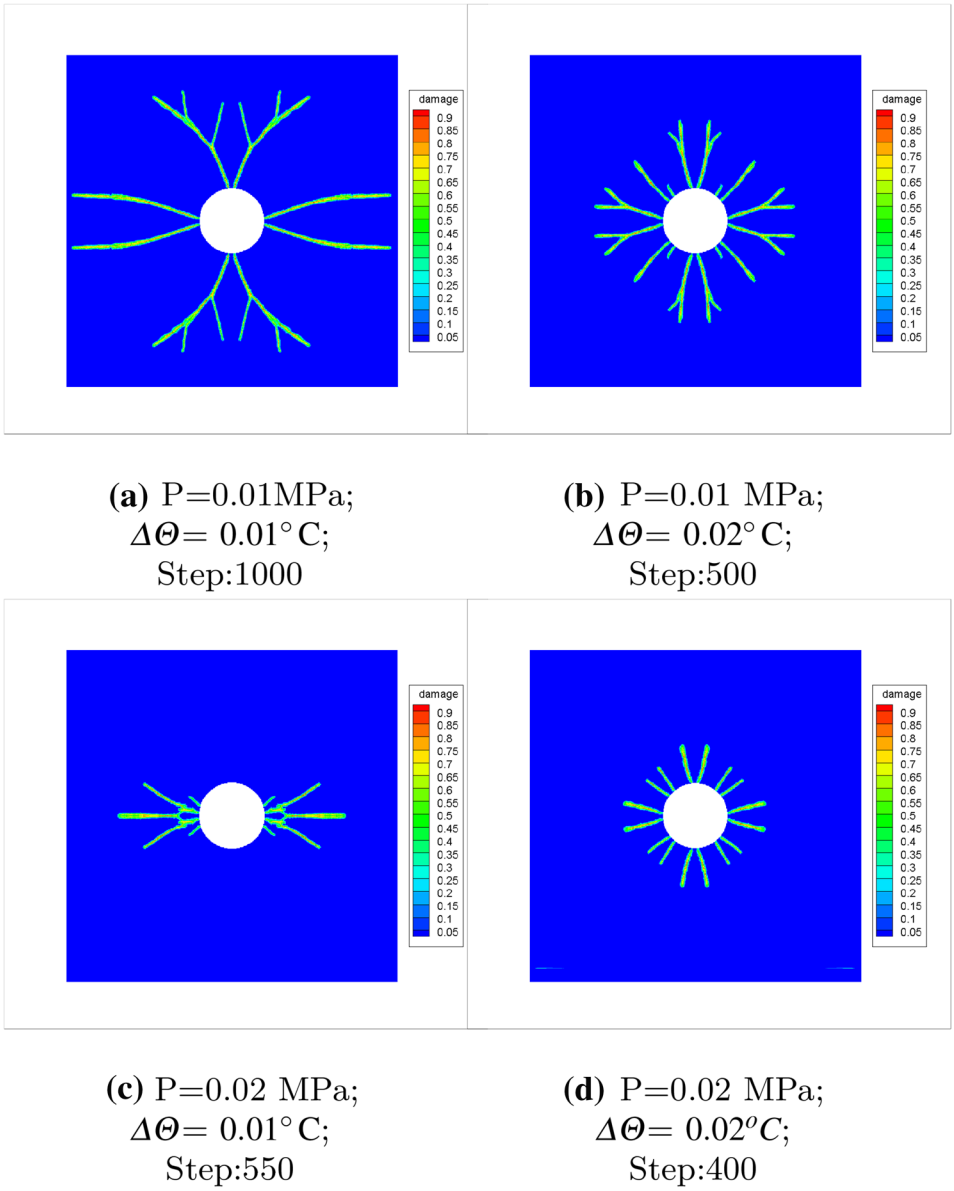

Fig. 23 Crack patterns at different thermo-mechanical conditions $\Theta_0 = -4\,^{\circ}\mathrm{C}$

bifurcation, and crack arrest of ice plate cracks, and the calculation results are clear and intuitive.

The bubbles in sea ice are randomly distributed, as is shown in Fig. 29. The porosity of ice affects the strength of ice, and we established ice models containing random bubbles. The crack propagation in ice models with different porosity p are shown in Figs. 30, 31, 32 and 33, The value of porosity p is chosen to be 0.01, 0.03, 0.1, and 0.12, respectively. From Figs. 30, 31, 32 and 33, we can see that the calculation method proposed in this study can simulate the crack initiation process under different porosity.

Finally, we discussed the relationship between porosity and ice tensile strength and compared the results in the literature. The comparison results are shown in Fig. 34. It can be seen from Fig. 34 that the tensile strength of ice is affected by porosity p, The variation trend of the simulation in this paper is consistent with the results in the literature, which verifies the practicability of the method in this paper.

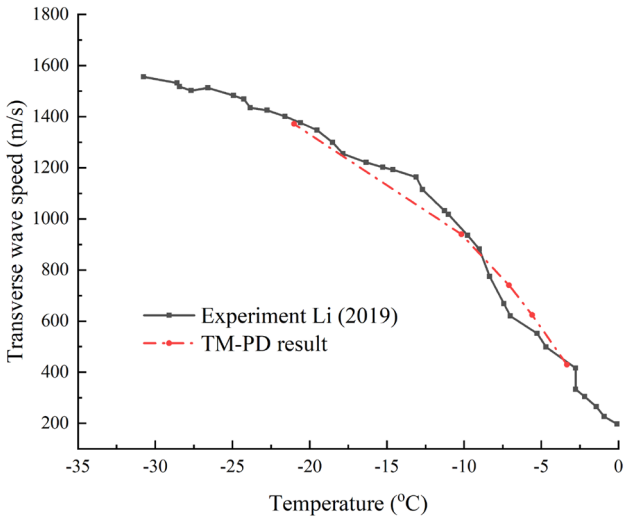

(a) Transverse wave

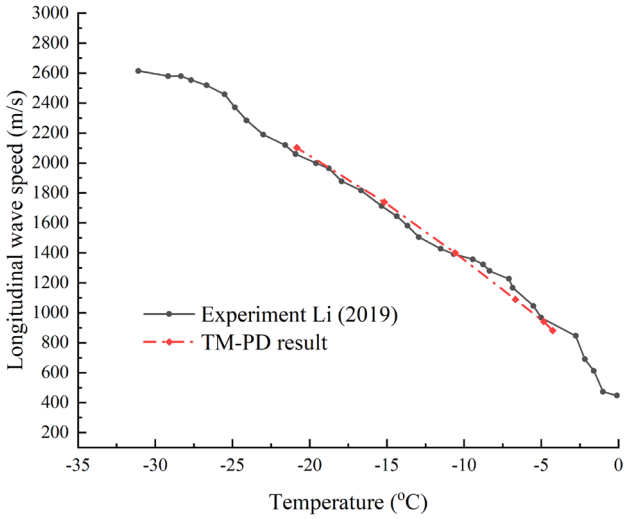

(b) Longitudinal wave

Fig. 24 Ice crack propagation speed in different thermal conditions

4 Conclusions

In this work, based on a thermo-mechanically coupled bond-based peridynamics, we developed a multi-scale model for heterogeneous ice. By employing this model, we have studied the crack propagation in ice under different thermo-mechanical conditions. In particular, we introduced the Weibull distribution into the t-bond equation of peridynamics and proposes a modeling method to deal with the nonuniform stress problems of ice materials such as lattice defects, slips, and dislocations, thereby realizing the transition from the microstructure of the ice material to the macrostructure. The main innovations and main conclusions drawn in this study are as follows:

1) By developing a heterogeneous elastic-strain softening peridynamic ice material model, we conducted comprehensive study the effects of ice microstructure, temperature, and stochastic uncertainty of grain size as well as the bond strength between ice particles on ice crack formation and fracture.
2) From the perspective of microscopic bond crack growth and fracture, we studied the crack propagation phenomenon of ice under different grain sizes, providing the explanation of the effect of grain size on ice crack propagation.
3) Unlike most of crack simulations that are using the peridynamics solution, which only consider mechanical loading conditions, the bond-based peridynamics solution presented in this paper considers the general thermo-mechanical loading conditions, and it simulates crack propagation in ice by considering both mechanical loading conditions as well as the influence of temperature.
4) The numerical simulation results obtained in this work are consistent with the crack formations obtained in the experimental observation and research of scholars. Under the compressive loading, we find that the basic

Fig. 25 Crack propagation process under the thermo-mechanical field

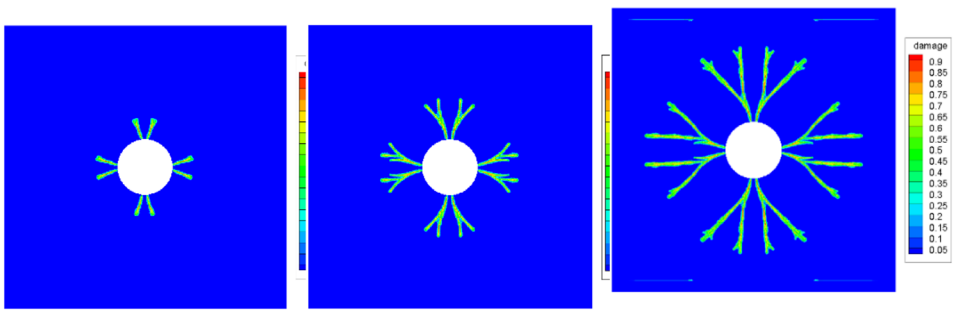

(a) Crack initiation: step 400

(b) Crack branching: step 500

(c) Crack termination: step 650

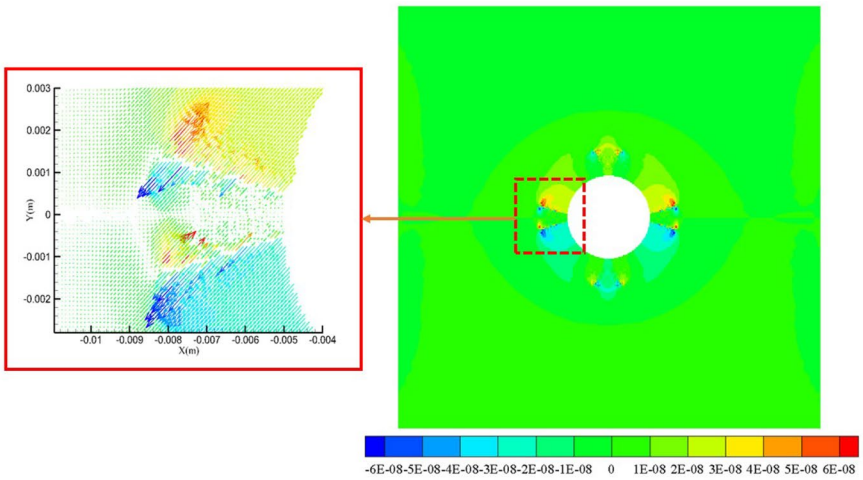

(a) Crack initiation: step 400

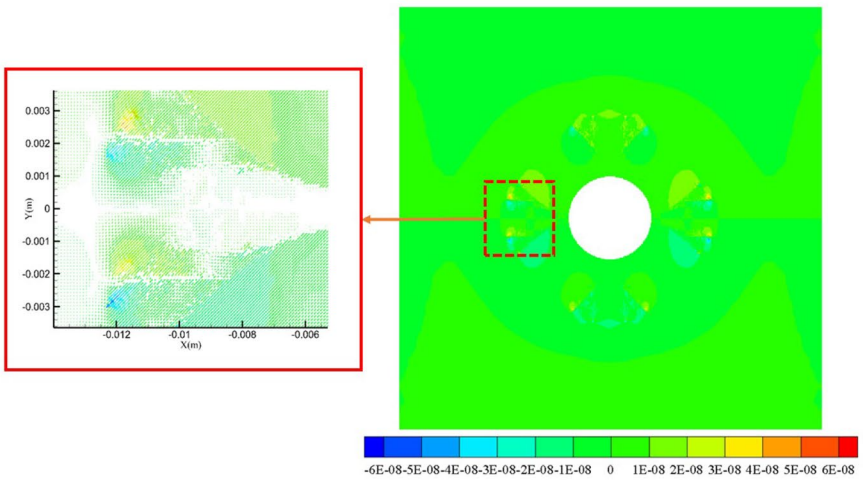

(b) Crack branching: step 500

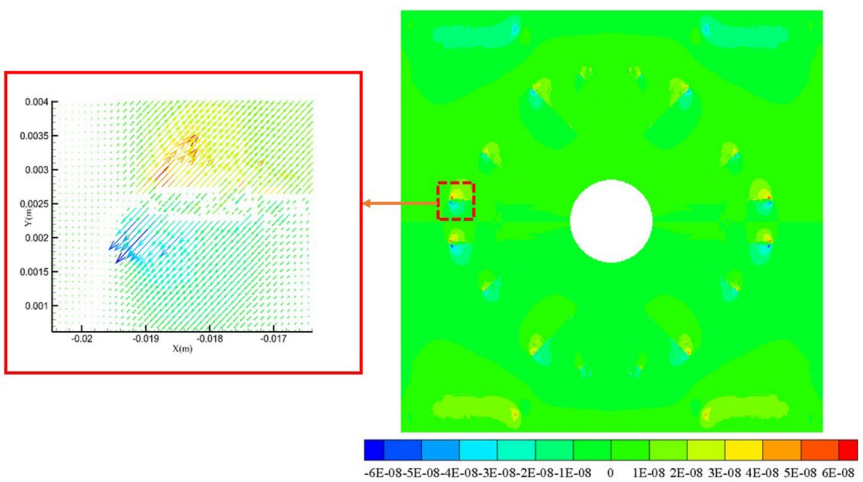

(c) Crack termination: step 650

Fig. 26 Detailed fracture morphology including particle velocity field at crack tip openings

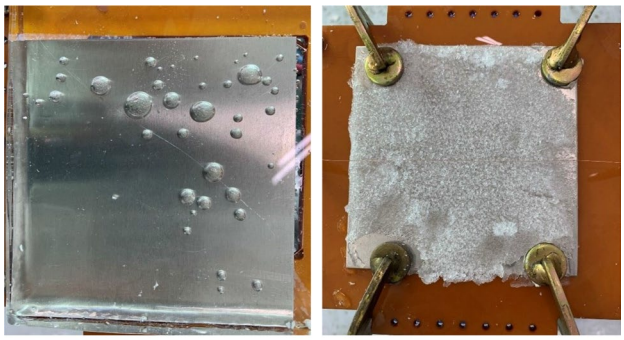

(a) Ice sample **(b)** Fixed method

Fig. 27 Experiment setup

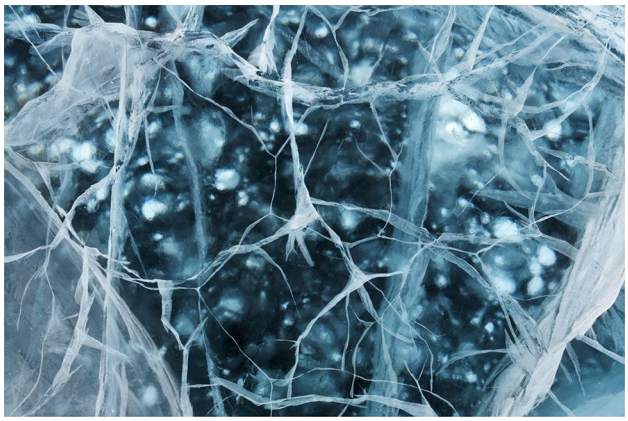

Fig. 29 Ice crack (Photo Courtesy: weekly-wrap-volume-89/ice-crack-2/)

crack failure mode is the wing-shaped cracks, and later multiple wing-shaped cracks may be merged, intersected, and connected, until the ice plate is disintegrated.

5) The thermo-mechanically coupled peridynamics ice model developed in this work is a comprehensive nonlocal ice material model, which takes into account the influence of the initial temperature of ice, the environmental temperature of ice, the size of ice crystals, and the heat conduction between material points. Thus, it can predict the ice fracture with high accuracy, including crack formations in the ice plates with different initial defects. At the same time, it can predict the critical load, the critical thermo-mechanical conditions, and fragility of ice plates with different initial defects.
6) Using the proposed method, we have calculated the crack formations in an ice plate with different initial defects. By comparing the effects of stress loading and thermo-mechanical coupling loading, we find that it is the instability of microcrack bifurcation leads to catastrophic fracture in ice.

Fig. 28 Comparison of crack pattern in the multi-bubble ice plate

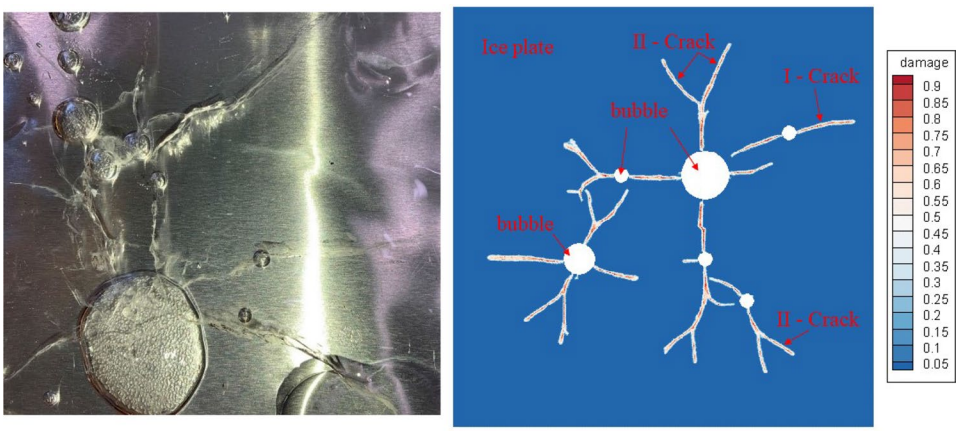

(a) Experimental result **(b)** Peridynamic result

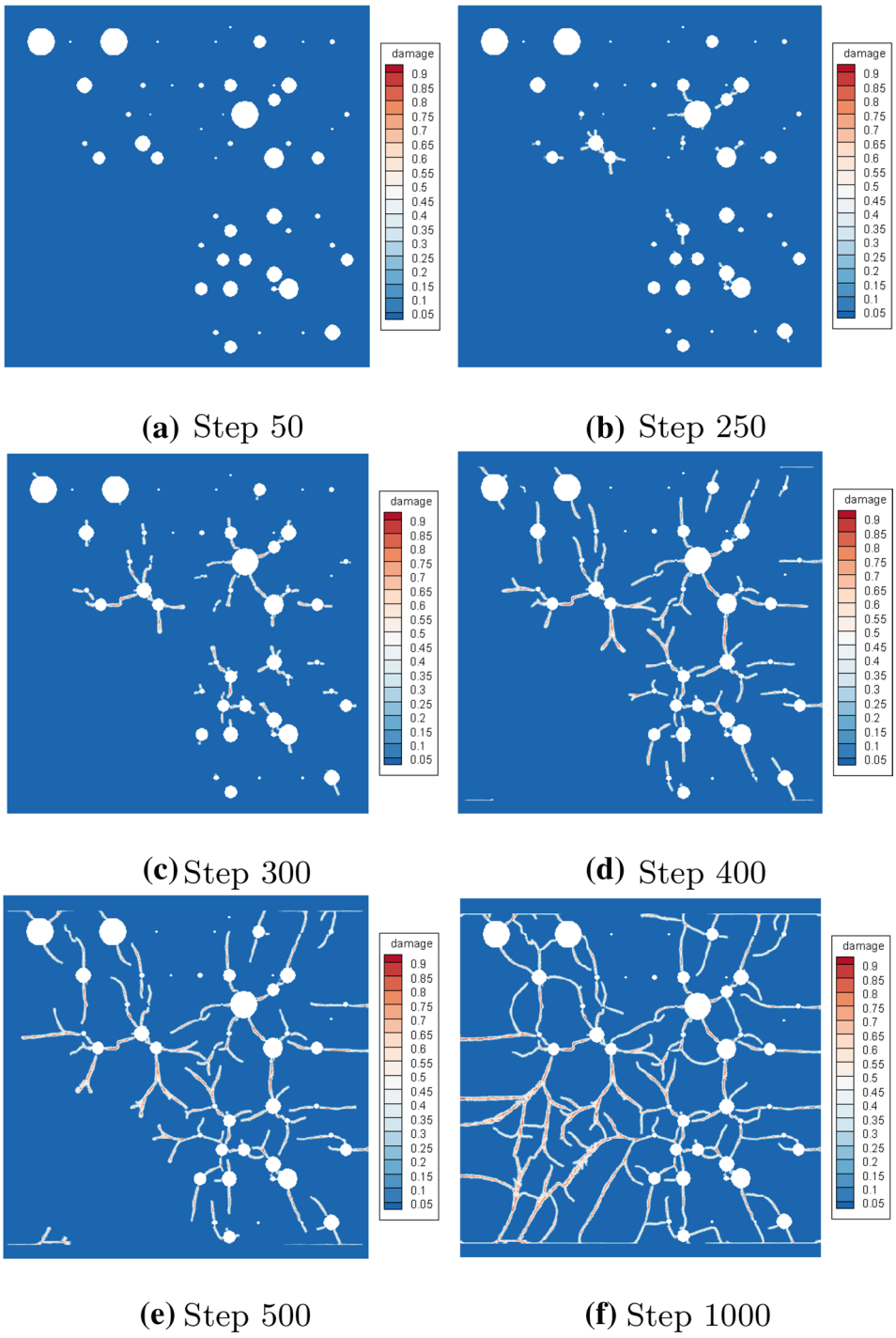

Fig. 30 The crack propagation in ice under case 1, $p = 0.01$

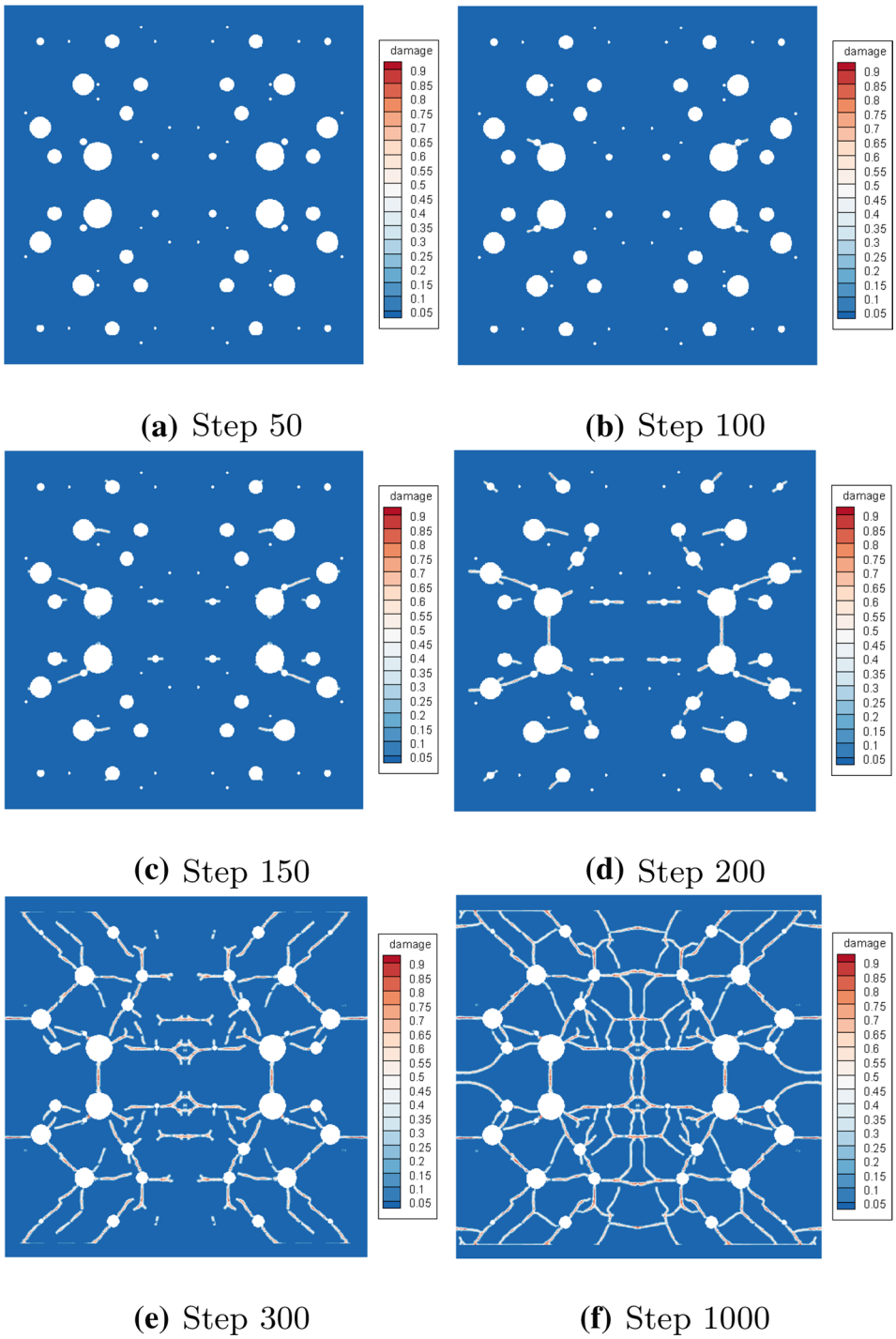

Fig. 31 The crack propagation in ice under case 1, $p = 0.03$

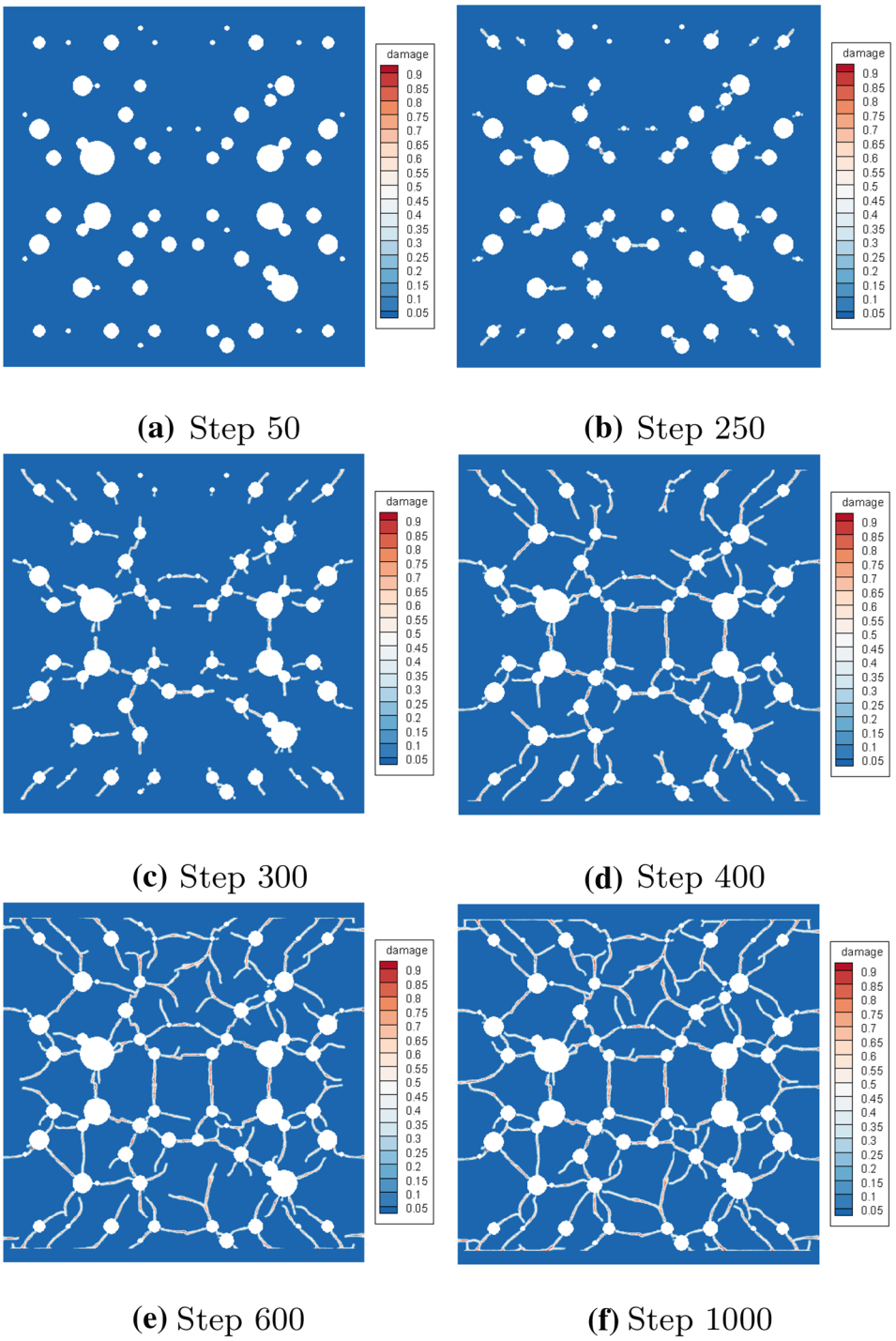

Fig. 32 The crack propagation in ice under case 2, $p = 0.1$

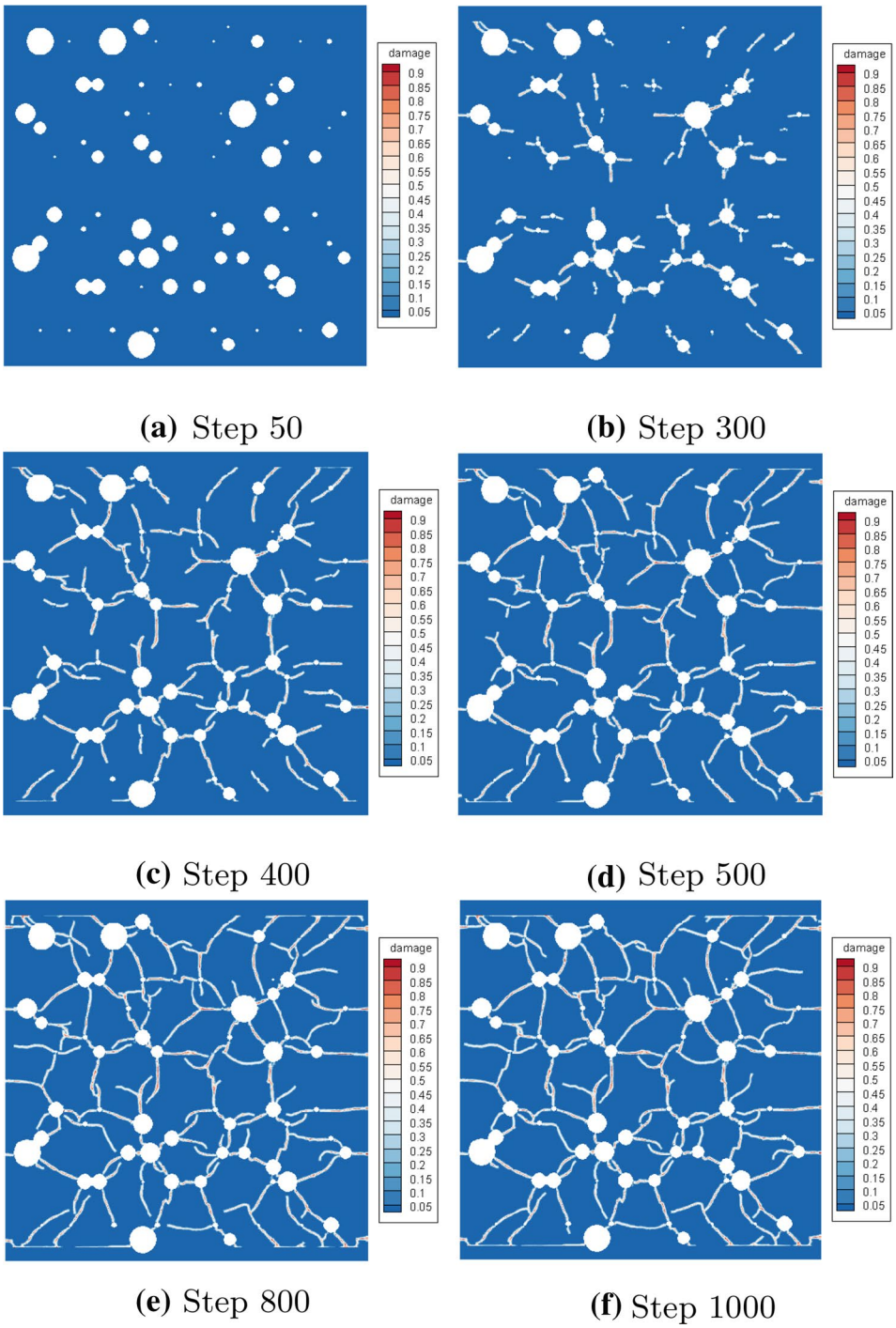

Fig. 33 The crack propagation in ice under case 2, $p = 0.12$

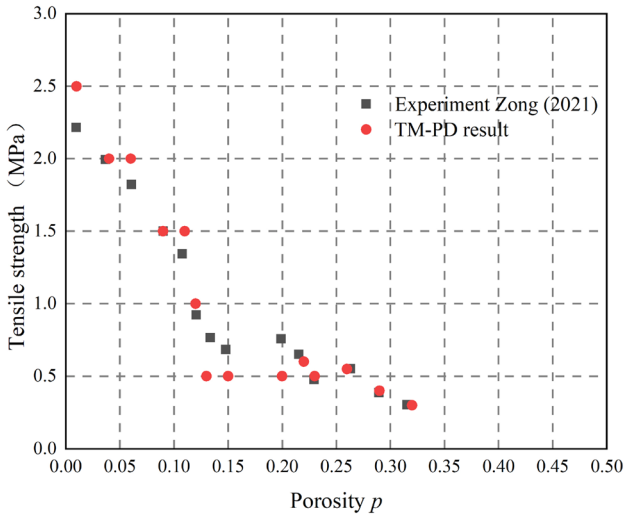

Fig. 34 The relationship between tensile strength and porosity [74]

Acknowledgements YS and YL were supported by the National Natural Science Foundation of China (Grant No. 51979049).

Author contributions YS: conceptualization, software, and writing; SL: methodology, supervision, and writing; YL: resources, analysis, and writing.

Declarations

Conflict of interest The authors declare that they have no known competing financial interests or personal relationships that could have appeared to influence the work reported in this paper.

References

1. Bergel G, Li S (2016) The total and updated Lagrangian formulation of state-based peridynamics. Comput Mech 58:351–370
2. Chen W, Gu X, Zhang Q, Xia X (2021) A refined thermo-mechanical fully coupled peridynamics with application to concrete cracking. Eng Fract Mech 242:107463
3. Chu D, Li X, Liu Z (2017) Study the dynamic crack path in brittle material under thermal shock loading by phase field modeling. Int J Fract 208(1):115–130
4. Cole D (2001) The microstructure of ice and its influence on mechanical properties. Eng Fract Mech 68(17–18):1797–1822
5. Cui P, Zhang AM, Wang S, Khoo B (2018) Ice breaking by a collapsing bubble. J Fluid Mech 841:287–309
6. Cui P, Zhang AM, Wang SP (2021) Shock wave emission and ice breaking effect of multiple interacting bubbles. Ocean Eng 234:109175
7. Cui P, Zhang AM, Wang SP, Liu YL (2020) Experimental study on interaction, shock wave emission and ice breaking of two collapsing bubbles. J Fluid Mech 897:A25
8. D'Antuono P, Morandini M (2017) Thermal shock response via weakly coupled peridynamic thermo-mechanics. Int J Solids Struct 129:74–89
9. Dempsey J (1991) The fracture toughness of ice. Ice-structure interaction. Springer, Berlin, pp 109–145
10. Dutta PK, Cole DM, Schulson EM, Sodhi DS (2003) Fracture study of ice under high strain rate loading. In: The thirteenth international offshore and polar engineering conference, OnePetro
11. Gao Y, Oterkus S (2021) Coupled thermo-fluid-mechanical peridynamic model for analysing composite under fire scenarios. Compos Struct 255:113006
12. Haynes FD (1978) Effect of temperature on the strength of snow-ice, vol 78. The Laboratory
13. Hibler WD (1979) A dynamic thermodynamic sea ice model. J Phys Oceanogr 9(4):815–846
14. Hooke RL, Hudleston PJ (1980) Ice fabrics in a vertical flow plane, Barnes ice cap, Canada. J Glaciol 25(92):195–214
15. Hunke E, Dukowicz J (1997) An elastic-viscous-plastic model for sea ice dynamics. J Phys Oceanogr 27(9):1849–1867
16. Ji SY, Shen H, Wang Z, Shen H, Yue Q (2005) A viscoelastic-plastic constitutive model with Mohr-coulomb yielding criterion for sea ice dynamics. Acta Oceanol Sin Engl Ed 24(4):54
17. Jones L, Vandeperre L, Haynes T, Wenman M (2020) Modelling of Weibull distributions in brittle solids using 2-dimensional peridynamics. Proc Struct Integr 28:1856–1874
18. Jones L, Vandeperre L, Haynes T, Wenman M (2020) Theory and application of Weibull distributions to 1D peridynamics for brittle solids. Comput Methods Appl Mech Eng 363:112903
19. Kan XY, Zhang AM, Yan J, Wu WB, Liu YL (2020) Numerical investigation of ice breaking by a high-pressure bubble based on a coupled BEM-PD model. J Fluids Struct 96:103016
20. Kilic B, Madenci E (2010) An adaptive dynamic relaxation method for quasi-static simulations using the peridynamic theory. Theor Appl Fract Mech 53(3):194–204
21. Lee R, Schulson E (1988) The strength and ductility of ice under tension. ASME J Offshore Mech Arct Eng 110(2):187–191
22. Li F, Kõrgesaar M, Kujala P, Goerlandt F (2020) Finite element based meta-modeling of ship-ice interaction at shoulder and midship areas for ship performance simulation. Mar Struct 71:102736
23. Li S, Simonsen C (2005) Meshfree simulations of ductile crack propagations. Int J Comput Methods Eng Sci Mech 6(1):1–19
24. Li Y (2019) Research on ice mechanical performance parameters based on ultrasonic. Taiyuan University of Technology, pp 109–145
25. Liu R, Xue Y, Lu X, Cheng W (2018) Simulation of ship navigation in ice rubble based on peridynamics. Ocean Eng 148:286–298
26. Liu R, Yan J, Li S (2020) Modeling and simulation of ice-water interactions by coupling peridynamics with updated Lagrangian particle hydrodynamics. Comput Part Mech 7(2):241–255
27. Lu W, Li M, Vazic B, Oterkus S, Oterkus E, Wang Q (2020) Peridynamic modelling of fracture in polycrystalline ice. J Mech 36(2):223–234
28. Madenci E, DM, Gu X (2019) Peridynamic least squares minimization. Comput Methods Appl Mech Eng 348:846–874
29. Madenci E, Barut A, Dorduncu M (2019) Peridynamic differential operator for numerical analysis. Springer International Publishing, Berlin
30. Madenci E, Oterkus E (2014) Peridynamic theory. Peridynamic theory and its applications. Springer, Berlin, pp 19–43
31. Mulmule S, Dempsey J (2000) LEFM size requirements for the fracture testing of sea ice. Int J Fract 102(1):85–98
32. Oterkus S, Madenci E (2017) Peridynamic modeling of fuel pellet cracking. Eng Fract Mech 176:23–37
33. Pan W, Tartakovsky AM, Monaghan J (2012) A smoothed-particle hydrodynamics model for ice-sheet and ice-shelf dynamics. J Glaciol 58(208):216–222
34. Peng Y, Zhang A, Ming F (2018) A thick shell model based on reproducing kernel particle method and its application in geometrically nonlinear analysis. Comput Mech 62(3):309–321

35. Peng YX, Zhang AM, Ming FR (2020) A 3D meshfree crack propagation algorithm for the dynamic fracture in arbitrary curved shell. Comput Methods Appl Mech Eng 367:113139
36. Peng YX, Zhang AM, Ming FR (2021) Numerical simulation of structural damage subjected to the near-field underwater explosion based on SPH and RKPM. Ocean Eng 222:108576
37. Peng YX, Zhang AM, Wang SP (2021) Coupling of WCSPH and RKPM for the simulation of incompressible fluid-structure interactions. J Fluids Struct 102:103254
38. Petrenko V, Whitworth R (1999) Physics of ice. OUP Oxford, Oxford
39. Petrovic J (2003) Review mechanical properties of ice and snow. J Mater Sci 38(1):1–6
40. Rabczuk T, Belytschko T (2007) A three-dimensional large deformation meshfree method for arbitrary evolving cracks. Comput Methods Appl Mech Eng 196(29–30):2777–2799
41. Rabczuk T, Ren H (2017) A peridynamics formulation for quasi-static fracture and contact in rock. Eng Geol 225:42–48
42. Rabczuk T, Ren H, Zhuang X (2019) A nonlocal operator method for partial differential equations with application to electromagnetic waveguide problem. Comput Mater Contin 59(1):31–55
43. Ren B, Li S (2010) Meshfree simulations of plugging failures in high-speed impacts. Comput Struct 88(15–16):909–923
44. Ren H, Zhuang X, Anitescu C, Rabczuk T (2019) An explicit phase field method for brittle dynamic fracture. Comput Struct 217:45–56
45. Ren H, Zhuang X, Rabczuk T (2016) A new peridynamic formulation with shear deformation for elastic solid. J Micromechanics Mol Phys 1(02):1650009
46. Ren H, Zhuang X, Rabczuk T (2017) Dual-horizon peridynamics: a stable solution to varying horizons. Comput Methods Appl Mech Eng 318:762–782
47. Ren H, Zhuang X, Rabczuk T (2020) A higher order nonlocal operator method for solving partial differential equations. Comput Methods Appl Mech Eng 367:113132
48. Ren H, Zhuang X, Rabczuk T, Zhu H (2019) Dual-support smoothed particle hydrodynamics in solid: variational principle and implicit formulation. Eng Anal Bound Elem 108:15–29
49. Schulson E (2001) Brittle failure of ice. Eng Fract Mech 68(17–18):1839–1887
50. Schulson E, Gratz E (1999) The brittle compressive failure of orthotropic ice under triaxial loading. Acta Mater 47(3):745–755
51. Schulson E, Hoxie S, Nixon W (1989) The tensile strength of cracked ice. Philos Mag A 59(2):303–311
52. Silling SA (2000) Reformulation of elasticity theory for discontinuities and long-range forces. J Mech Phys Solids 48(1):175–209
53. Silling SA, Epton M, Weckner O, Xu J, Askari E (2007) Peridynamic states and constitutive modeling. J Elast 88(2):151–184
54. Song Y, Li S, Zhang S (2021) Peridynamic modeling and simulation of thermo-mechanical de-icing process with modified ice failure criterion. Def Technol 17(1):15–35
55. Song Y, Liu R, Li S, Kang Z, Zhang F (2020) Peridynamic modeling and simulation of coupled thermomechanical removal of ice from frozen structures. Meccanica 55(4):961–976
56. Song Y, Yan J, Li S, Kang Z (2019) Peridynamic modeling and simulation of ice craters by impact. Comput Model Eng Sci 121(2):465–492
57. Sun P, Colagrossi A, Marrone S, Zhang A (2016) Detection of Lagrangian coherent structures in the SPH framework. Comput Methods Appl Mech Eng 305:849–868
58. Sun P, Ming F, Zhang A (2015) Numerical simulation of interactions between free surface and rigid body using a robust SPH method. Ocean Eng 98:32–49
59. Timco G, Weeks W (2010) A review of the engineering properties of sea ice. Cold Reg Sci Technol 60(2):107–129
60. Wang P, Meng Z, Zhang AM, Ming FR, Sun PN (2019) Improved particle shifting technology and optimized free-surface detection method for free-surface flows in smoothed particle hydrodynamics. Comput Methods Appl Mech Eng 357:112580
61. Wang P, Zhang AM, Ming F, Sun P, Cheng H (2019) A novel non-reflecting boundary condition for fluid dynamics solved by smoothed particle hydrodynamics. J Fluid Mech 860:81–114
62. Wang Q, Wang Y, Zan Y, Lu W, Bai X, Guo J (2018) Peridynamics simulation of the fragmentation of ice cover by blast loads of an underwater explosion. J Mar Sci Technol 23(1):52–66
63. Wang Y, Zhou X, Kou M (2018) A coupled thermo-mechanical bond-based peridynamics for simulating thermal cracking in rocks. Int J Fract 211(1):13–42
64. Wang Y, Zhou X, Kou M (2018) Peridynamic investigation on thermal fracturing behavior of ceramic nuclear fuel pellets under power cycles. Ceram Int 44(10):11512–11542
65. Wang Y, Zhou X, Kou M (2019) An improved coupled thermo-mechanic bond-based peridynamic model for cracking behaviors in brittle solids subjected to thermal shocks. Eur J Mech A Solids 73:282–305
66. Xiong W, Wang C, Wang C, Ma Q, Xu P (2020) Analysis of shadowing effect of propeller-ice milling conditions with peridynamics. Ocean Eng 195:106591
67. Xu Y, Kujala P, Hu Z, Li F, Chen G (2020) Numerical simulation of level ice impact on landing craft bow considering the transverse isotropy of Baltic Sea ice based on XFEM. Mar Struct 71:102735
68. Xue Y, Liu R, Liu Y, Zeng L, Han D (2019) Numerical simulations of the ice load of a ship navigating in level ice using peridynamics. CMES Comput Model Eng Sci 121(2):523–550
69. Ye L, Guo C, Wang C, Wang C, Chang X (2020) Peridynamic solution for submarine surfacing through ice. Ships Offshore Struct 15(5):535–549
70. Ye L, Wang C, Chang X, Zhang H (2017) Propeller-ice contact modeling with peridynamics. Ocean Eng 139:54–64
71. Yu H, Li S (2020) On energy release rates in peridynamics. J Mech Phys Solids 142:104024
72. Yu H, Li S (2021) On approximation theory of nonlocal differential operators. Int J Numer Methods Eng 122:6984–7012
73. Zhang Y, Deng H, Deng J, Liu C, Yu S (2020) Peridynamic simulation of crack propagation of non-homogeneous brittle rock-like materials. Theor Appl Fract Mech 106:102438
74. Zong Z (2022) A random pore model of sea ice for predicting its mechanical properties. Cold Reg Sci Technol 195:103473